J. Fluid Mech. (2021), *vol*. 918, A13, doi:10.1017/jfm.2021.279

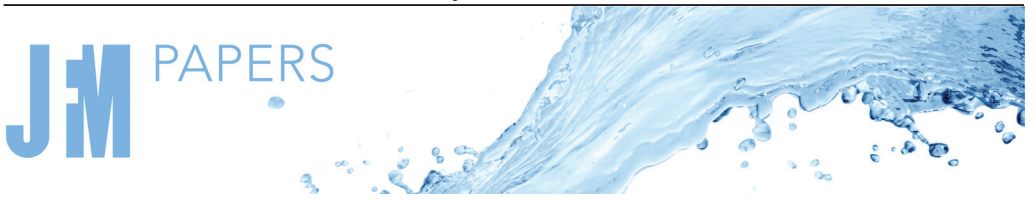

Large-to-small scale frequency modulation analysis in wall-bounded turbulence via visibility networks

Giovanni Iacobello[1],†, Luca Ridolfi[2] and Stefania Scarsoglio[1]

[1]Department of Mechanical and Aerospace Engineering, Politecnico di Torino, 10129 Turin, Italy

[2]Department of Environmental, Land and Infrastructure Engineering, Politecnico di Torino, 10129 Turin, Italy

(Received 13 November 2020; revised 3 March 2021; accepted 24 March 2021)

Scale interaction is studied in wall-bounded turbulence by focusing on the frequency modulation (FM) mechanism of the large scales on small-scale velocity fluctuations. Different from the analysis of amplitude modulation (AM), FM has been less investigated owing to the difficulty of developing robust tools for broadband signals. To tackle this issue, the natural visibility graph approach is proposed in this work to map the full velocity signals into complex networks. We show that the network degree centrality is able to capture the signal structure at local scales directly from the full signal, thereby quantifying FM. Velocity signals from numerically-simulated turbulent channel flows and an experimental turbulent boundary layer are investigated at different Reynolds numbers. A correction of Taylor's hypothesis for time series is proposed to overcome the overprediction of near-wall FM obtained when local mean velocity is used as the convective velocity. Results provide network-based evidence of the large-to-small FM features for all the three velocity components in the near-wall region, with a reversal mechanism emerging far from the wall. Additionally, scaling arguments, in view of the quasi-steady quasi-homogeneous hypothesis, are discussed, and a delay time between the large and small scales is detected that is very close to the characteristic time of the near-wall cycle. Results show that the visibility graph is a parameter-free tool that turns out to be effective and robust to detect FM in different configurations of wall-bounded turbulent flows. Based on the present findings, the visibility network-based approach can represent a reliable tool to systematically investigate scale interaction mechanisms in wall-bounded turbulence.

Key words: turbulent boundary layers

† Email address for correspondence: giovanni.iacobello@polito.it

1. Introduction

The characterization and modelling of wall-bounded turbulent flows is of paramount importance in physics and engineering (Marusic, Mathis & Hutchins 2010). Organized motions, in particular, play a crucial role in wall-bounded turbulence analysis, because they are associated with high-energy levels and are directly involved in transport processes, which make them preferential targets for flow control strategies (Jiménez 2018). Coherent streaks are recognized as the dominant flow structures very close to the wall, and are characterized by a distinctive (inner) peak in the spectrogram of the streamwise velocity fluctuations, u, within the buffer layer (Jiménez 2018). The investigation of high-Reynolds-number experiments and simulations also reveal the formation of large-scale motions (LSMs) and very-large-scale motions (VLSMs) that reside in the log region (Smits, McKeon & Marusic 2011), whose presence is detected by the appearance of another (outer) peak in the (pre-multiplied) energy spectrogram of the streamwise velocity fluctuations (Hutchins & Marusic 2007*b*; Monty *et al.* 2009; Peruzzi *et al.* 2020). The wall-normal location in wall units (i.e. made dimensionless by the mean friction velocity, U_τ, and the fluid kinematic viscosity, ν), $y^+ = yU_\tau/\nu$, of the inner peak is conventionally assumed to be fixed at $y^+ = 15$, while the position of the outer peak increases with the frictional Reynolds number, Re_τ, as $y^+ \approx 3.9Re_\tau^{1/2}$ (Mathis, Hutchins & Marusic 2009*a*).

In addition to the effect of the Reynolds number, some differences emerge from the comparison of different canonical wall-bounded turbulent flows. While near-wall statistics (such as the mean velocity profile) agree well in channel, pipe and boundary layer flows, the features of the large scales depend on the flow configuration (Balakumar & Adrian 2007; Monty *et al.* 2007; Mathis *et al.* 2009*b*; Monty *et al.* 2009; Chernyshenko 2020). In particular, spectral analyses of internal and external flows have revealed that the very-large scales tend to be longer for channel and pipe flows than boundary layer flows, although they appear to be qualitatively similar (Balakumar & Adrian 2007; Monty *et al.* 2009). Such large-scale differences are expected to increase for larger Reynolds numbers as energetic contributions resulting from VLSM increases with the Reynolds number.

The investigation of higher Reynolds number data has progressively revealed novel developments and questions concerning the interaction between the small-scale turbulence (whose spectral peak occurs in the proximity of the wall) and LSMs (whose spectral peak resides far from the wall). Insights on scale interaction were initially reported by Brown & Thomas (1977) and Bandyopadhyay & Hussain (1984), who observed a modulation mechanism on the (near-wall) small scales by the large turbulent scales. Later, Hutchins & Marusic (2007*b*) provided further evidence of a top-down footprint and an AM phenomenon by the large scales residing in the log region on the near-wall (small-scale) dynamics. With the aim to illustrate such an inter-scale mechanism, figure 1(*a*) shows a schematic of a wall-bounded turbulent flow in a streamwise-vertical plane, where uniform momentum regions arising from LSM and VLSM (highlighted as dark- and light-blue structures) entail large-scale fluctuations, u_{LS} (see red lines). Figure 1(*a*) is drawn following the current picture of the kinematics of turbulent scales and their interaction in wall-bounded turbulence (e.g. see Ganapathisubramani *et al.* 2012; Baars, Hutchins & Marusic 2017). The turbulent flow field can be decomposed as $u(x, y, z, t) = u_{LS}(x, y, z, t) + u_{SS}(x, y, z, t)$, where u_{SS} are small-scale fluctuations (see black signals), while x, y, z are the streamwise, vertical and spanwise directions, respectively, and t is the time. Figure 1(*a*) also highlights the top-down footprint of the large scales, being the two u_{LS} signals (red lines) positively correlated with each other (eventually accounting for the inclination of the large scales Marusic & Heuer 2007).

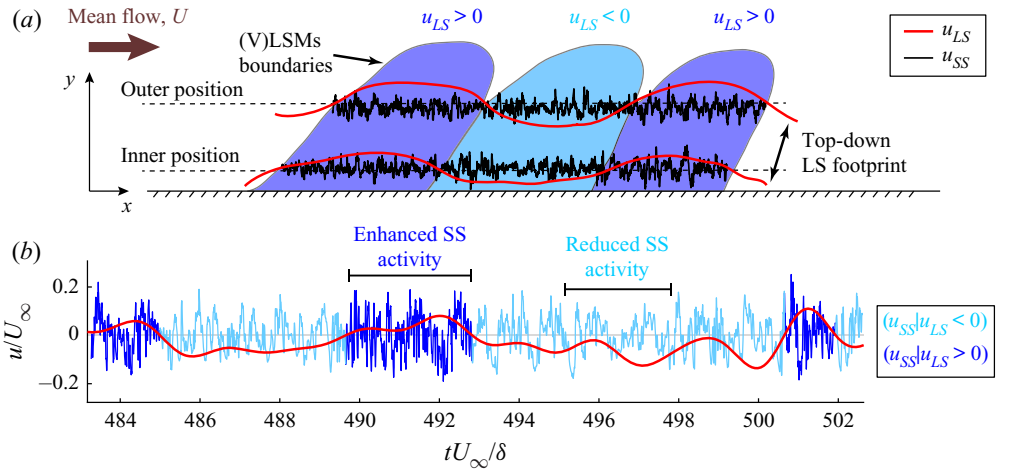

Figure 1. (*a*) Schematic of a wall-bounded turbulent flow in the (*x*–*y*) plane, showing three alternating LSM and VLSM structures of uniform large-scale momentum, $u_{LS} \lessgtr 0$. Two pairs of time series of u_{LS} and u_{SS} are also depicted as red and black lines, respectively, at two wall-normal locations (referred to as the inner and outer positions). (*b*) Small-scale, u_{SS}, and large-scale, u_{LS}, streamwise velocity fluctuations at $y^+ \approx 10$, shown as blue and red lines, respectively, where the light- and dark-blue portions of u_{SS} correspond to intervals of $u_{LS} < 0$ and $u_{LS} > 0$, respectively. The velocity series is extracted from an experimental turbulent boundary layer at $Re_\tau = 14\,750$ (Marusic 2020) in the range $tU_\infty/\delta = 483$–503, where U_∞ and δ are the free stream velocity and boundary layer thickness, respectively. Two intervals of the signal (i.e. $490 < tU_\infty/\delta < 493$ and $495 < tU_\infty/\delta < 498$), in which the small scales display enhanced or reduced activity, are also indicated.

A modulation of the amplitude of the small scales caused by the large scales implies that high or low values of u_{LS} correspond to (on average) high or low values of u_{SS}. This mechanism can be observed in figure 1(*b*), which shows time intervals of u_{LS} and u_{SS} at $y^+ \approx 10$ in an experimental turbulent boundary layer. An increase of the local amplitude of the small-scale signal (see dark-blue intervals) is discernible during positive large-scale velocity fluctuations, $u_{LS} > 0$, and, *vice versa*, a damping of the small-scale amplitudes (light-blue intervals) is evident during negative large-scale velocity fluctuations, $u_{LS} < 0$.

Mathis *et al.* (2009*a*) quantified this AM by correlating u_{LS} with the large-scale-filtered envelope of u_{SS} at different wall-normal coordinates. The authors observed an AM (as shown in figure 1*b*) only close to the wall (approximatively below the centre of the log region), while a reversed AM mechanism – i.e. an u_{SS} amplitude increase under $u_{LS} < 0$ and an u_{SS} amplitude decrease under $u_{LS} > 0$ – occurred far from the wall. Further studies on turbulent boundary layers have suggested that a modulation mechanism does actually take place only in the near-wall region, while different mechanisms occur in the log and wake regions. In particular, the behaviour of the scale interaction away from the wall has been explained either through a preferential arrangement of the small scales – i.e. an alignment of the small-scale turbulence with internal shear layers that separate zones of large-scale uniform momentum (Hutchins 2014; Baars *et al.* 2017) – or as an effect of variations in the mean strain and in the shear-driven production (Agostini & Leschziner 2019).

Based on the insights from Hutchins & Marusic (2007*b*) and Mathis *et al.* (2009*a*), AM has been widely investigated for several flow configurations and Reynolds numbers, both experimentally (e.g. see Mathis *et al.* 2009*b*; Schlatter & Örlü 2010; Guala, Metzger & McKeon 2011; Ganapathisubramani *et al.* 2012; Talluru *et al.* 2014; Baars *et al.* 2015;

Duvvuri & McKeon 2015; Squire *et al.* 2016; Baars *et al.* 2017; Pathikonda & Christensen 2017; Basley, Perret & Mathis 2018; Pathikonda & Christensen 2019) and via numerical simulations (e.g. see Chung & McKeon 2010; Bernardini & Pirozzoli 2011; Agostini & Leschziner 2014; Agostini, Leschziner & Gaitonde 2016; Anderson 2016; Hwang *et al.* 2016; Yao, Huang & Xu 2018; Agostini & Leschziner 2019; Dogan *et al.* 2019). Furthermore, findings on scale interactions have fostered the development of predictive models for near-wall turbulence that explicitly account for the footprint and AM by the large scales on the small scales (Marusic *et al.* 2010; Mathis, Hutchins & Marusic 2011; Mathis *et al.* 2013; Baars, Hutchins & Marusic 2016; Wu, Christensen & Pantano 2019). It should be noted that, although large-scale spectral features do not match between internal and external flows, similar AM results have been found for channel, pipe and boundary layer flows at similar Re_τ values (Mathis *et al.* 2009*b*), which suggest a similar scale-interaction mechanism is at play in all configurations.

In addition to AM, small-scale turbulence has also been found to change its instantaneous (i.e. local) frequency during intervals of positive or negative u_{LS}, namely the large scales affect the small scales through a frequency modulation (FM) mechanism (Ganapathisubramani *et al.* 2012; Baars *et al.* 2015; Fiscaletti, Ganapathisubramani & Elsinga 2015). However, only a few investigations to quantify FM in wall-bounded turbulence have been carried out so far (Ganapathisubramani *et al.* 2012; Baars *et al.* 2015, 2017; Pathikonda & Christensen 2017; Awasthi & Anderson 2018; Tang & Jiang 2018; Pathikonda & Christensen 2019) when compared with the vast literature on AM and its application into predictive models. One of the main reasons for this literature imbalance resides on the difficulty to produce robust methodologies to quantify FM in broadband signals, as well as the difficulty to effectively capture instantaneous frequencies in a signal.

With the aim to quantify FM in the context of a wall-bounded turbulence scale interaction, two methodologies have been proposed so far. Ganapathisubramani *et al.* (2012) proposed a peak–valley approach, following the idea that the local frequency is proportional to the number of maxima and/or minima per unit length of the series. The peak–valley approach was applied to streamwise u_{SS} signals from experimental measurements in a turbulent boundary layer at $Re_\tau = \delta U_\tau/\nu = 14\,150$ (where δ is the boundary layer thickness). Similar to AM, the authors found a relevant FM of the small scales in the near-wall region in which higher frequencies correspond to large (positive) u_{LS} values while lower frequencies correspond to low (negative) u_{LS} values. However, different from AM, substantial FM was observed only up to $y^+ \approx 100$. As an example of this FM mechanism, in figure 1(*b*), a rapidly fluctuating u_{SS} activity can be seen during positive u_{LS} (dark-blue intervals) rather than negative u_{LS} (light blue intervals). Despite its conceptual simplicity, the main drawback of the peak–valley approach is the need of a signal discretization into sub-intervals of arbitrary spacing to quantify the number of maxima and minima within each sub-interval. The choice of the size of the signal partition into sub-intervals is non-trivial and requires a trade-off between too short or too large intervals that can affect the results. Moreover, as pointed out by Baars *et al.* (2015), the short-time partitioning of the peak–valley approach makes it less applicable if a focus on temporal shifts in AM and FM is required.

An alternative approach to quantify FM and effectively account for time shifts was then proposed by Baars *et al.* (2015), who exploited wavelet analysis to extract from the velocity time series a new signal that is representative of the local frequency variations at the small scales. The authors performed a time–frequency analysis of the streamwise velocity, in which a time series – representative of the small-scale instantaneous frequency – was obtained by evaluating the first spectral moment of the wavelet power spectrum, namely an

average energetic contribution at each time for the range of (high) frequencies pertaining the small scales (Baars *et al.* 2015). The first spectral moment was eventually long-pass filtered to retain only its large-scale component, and correlated with u_{LS} to quantify FM (similar to the AM technique proposed by Mathis *et al.* 2009*a*).

The wavelet-based procedure was applied to experimental streamwise velocity time series measured at different wall-normal locations from a turbulent boundary layer at $Re_\tau = 14\,750$ (Baars *et al.* 2015). The authors showed positive correlations up to the centre of the log region, which meant that higher and lower frequencies in u_{SS} were detected under $u_{LS} > 0$ and $u_{LS} < 0$, respectively. Almost zero correlations were observed, instead, for higher wall-normal locations up to the boundary layer intermittent region, where negative correlation values were detected. The near-wall FM found by Baars *et al.* (2015) is in accordance with the outcomes from Ganapathisubramani *et al.* (2012), but the y^+ coordinate above which FM was found to be almost absent is larger by using the wavelet-based approach ($y^+ \approx 470$) compared with that obtained by the peak–valley approach ($y^+ \approx 100$), although the Re_τ values were rather similar. Furthermore, a phase lead of the small-scale amplitude and frequency was found in the near-wall with respect to the large-scale signals, and – in accordance with previous studies (Bandyopadhyay & Hussain 1984; Guala *et al.* 2011) – a much larger lead was detected for the small-scale amplitudes than for frequency. Although the FM has been accepted as a near-wall mechanism, the interaction mechanism in terms of FM between the small and large scales in the log and wake regions has not been completely clarified, in particular, the precise wall-normal coordinate at which the small-scale frequency is no longer affected by the large scales needs to be determined.

So far, the wavelet-based technique by Baars *et al.* (2015) has been exploited as the main tool to quantify FM in wall-bounded turbulence. Different flow configurations have been explored in terms of FM, such as experimental smooth-wall turbulent boundary layers via hot-wire measurements (Baars *et al.* 2017) and particle image velocimetry (Pathikonda & Christensen 2019), experimental boundary layers in the presence of wall roughness (Pathikonda & Christensen 2017; Tang & Jiang 2018), as well as large-eddy simulation of a turbulent channel flow with spanwise heterogeneity (Awasthi & Anderson 2018). These works highlighted that, despite the specific quantitative differences, near-wall FM is present both for smooth and rough walls, as well as for several Reynolds numbers. However, despite its preferred employment for quantifying FM, the wavelet-based approach presents some criticalities. First, as discussed by Baars *et al.* (2015), the choice of the mother wavelet can have an impact on the results because different frequency resolutions are gained from different mother wavelets. Moreover, the procedure necessitates multiple filtering operations that demand the choice of an appropriate frequency filter value. In particular, a frequency threshold is required both in the computation of the first spectral moment of the wavelet power spectrum (which involves a numerical integration) and in the long-pass filtering of the first spectral moment. Therefore, different from the peak–valley approach of Ganapathisubramani *et al.* (2012), in which maxima and minima are counted, the wavelet-based approach intrinsically requires several procedural steps and assumptions that need to be carefully handled.

In this work, a novel approach to study FM in wall-bounded turbulence is put forward with a twofold aim: (i) to propose a non-parametric and robust methodology to extract local frequency changes in a signal; and (ii) to show its effectiveness for two wall-bounded turbulence configurations, as well as to report novel insights that can help to further shed light on the large–small-scale interaction. Our methodology relies on the natural

visibility graph (NVG) approach proposed by Lacasa *et al.* (2008), which is used to map a signal into a network by exploiting a geometrical criterion. Thanks to its simplicity of implementation, the NVG has been widely employed in a variety of research areas such as, among many others, economy, biomedicine and geophysics (Zou *et al.* 2018). In particular, visibility-based investigations have been carried out in fluid mechanics to study jets and fires (Charakopoulos *et al.* 2014; Murugesan, Zhu & Li 2019; Tokami *et al.* 2020), wall-bounded turbulent flows (Liu, Zhou & Yuan 2010; Iacobello, Scarsoglio & Ridolfi 2018*b*), passive scalar plumes (Iacobello *et al.* 2018*a*, 2019*a*) and turbulent combustors (Murugesan & Sujith 2015, 2016; Singh *et al.* 2017).

In spite of its simplicity, the NVG approach (defined in § 2.1) has been shown to be a powerful tool in capturing important features of the mapped signal (such as the occurrence of extreme events) and as a reliable indicator of the transition between different flow dynamics (Iacobello, Ridolfi & Scarsoglio 2021). Here we show that the degree centrality, which is one of the simplest network metrics, is much more sensitive to the small-scale spectral energy variations than their large-scale counterpart (2.2). Accordingly, the network degree is viewed as a metric that is able to inherit the local frequency variations in a signal (2.3), without any *a priori* assumption (e.g. signal filtering). Therefore, the NVG approach can be directly used to study the full velocity signals rather than the small-scale component.

The proposed NVG approach is used to analyse the time series (§ 3.2) from an experimental smooth-wall zero-pressure-gradient turbulent boundary layer ($Re_\tau = 14\,750$, Marusic 2020), and the spatial series – namely one-dimensional (1-D) signals along spatial transects at a fixed time (§ 3.1) – from two direct numerical simulations (DNSs) of smooth-wall incompressible turbulent channel flows ($Re_\tau \approx 5200$ and $Re_\tau = 1000$, Lee & Moser 2015; Graham *et al.* 2016). In this regard, for simplicity, we refer FM to indicate both temporal and spatial frequency (i.e. wavenumber) modulation, where the former applies to the time series while the latter to the spatial series. A comparative FM analysis is performed by highlighting the differences and similarities between outcomes from the two wall-bounded turbulence set-ups for the streamwise velocity (§ 4.1). In particular, the effect of different Reynolds numbers is examined, and the application of Taylor's hypothesis to the time series is discussed by proposing a convection velocity that compensates for the overprediction of the modulation in the near-wall region. Moreover, FM results are examined, in view of the quasi-steady quasi-homogeneous theory, in terms of degree centrality scaling with respect to the large-scale velocity values (§ 4.2). The analysis is then extended to the wall-normal and spanwise velocities of the channel flow (§ 4.3), and the time and space shifts are eventually investigated for all the three velocity components (§ 4.4). Finally, we provide a discussion on some general features of the visibility approach (§ 5) as well as concluding remarks (§ 6).

2. Visibility-based analysis of frequency modulation

2.1. *Definition of visibility graph*

Visibility graphs represent a widely employed technique to map a discrete signal in a network. The idea behind the visibility graph approach is to assign a node of the network to each datum in the signal, and activate a link between two nodes if a geometrical criterion is satisfied. The main variant is the NVG, which is based on a convexity criterion (Lacasa *et al.* 2008). Geometrically, two nodes in an NVG (corresponding to two points in the signal) are linked if the straight line connecting the two points lies above any other in-between data. Figure 2(*a*, lower diagram) shows an example of a short series, $s_i \equiv s(\chi_i)$,

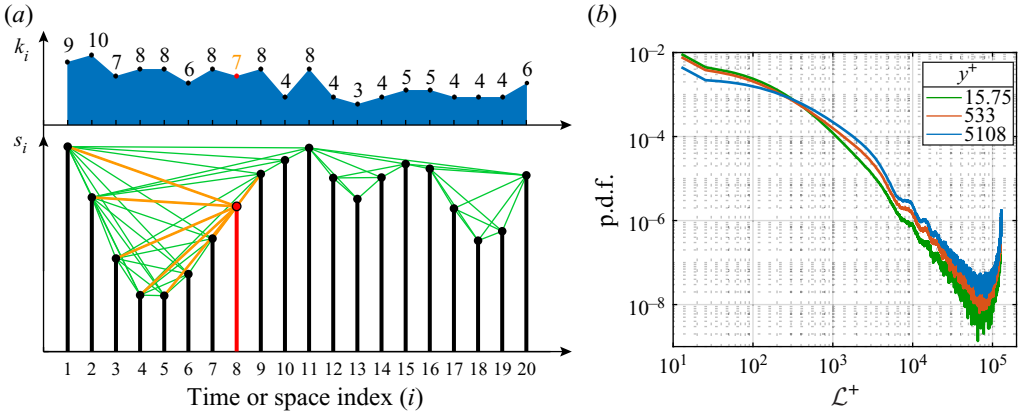

Figure 2. (*a*) The lower diagram shows an example of a signal, $s_i \equiv s(\chi_i)$, and the corresponding visibility network, where nodes are depicted as black filled circles and links as green lines. In particular, the node $i = 8$ and its links are highlighted in orange. The degree values for each node, k_i, are also shown in the upper diagram. (*b*) Probability density function (PDF) of the link length evaluated on the network built from the streamwise velocity, $u(x)$, in a turbulent channel flow at $Re_\tau \approx 5200$. The link length is expressed in wall units as $\mathcal{L}^+ = |i - j|\Delta x^+$, where i and j are the indices of two connected nodes and $\Delta x^+ = 12.7$ (see § 3.1).

for the independent variable χ_i (i.e. a time or space coordinate), comprising $N = 20$ observations, illustrated as vertical bars. Nodes and links in figure 2(*a*) are depicted as filled circles at the tip of each bar and green straight lines, respectively. A representative node is highlighted in red and its links are reported in orange.

The NVG criterion applied to a generic signal, $s(\chi)$, can be formally written as

$$s(\chi_n) < s(\chi_j) + (s(\chi_i) - s(\chi_j))\frac{\chi_j - \chi_n}{\chi_j - \chi_i}, \quad i, j = 1, \ldots, N, \tag{2.1}$$

for any χ_n (i.e. time or space coordinate) such that $\chi_i < \chi_n < \chi_j$ (Lacasa *et al.* 2008). The corresponding visibility network is represented through the adjacency (binary) matrix $\boldsymbol{A}$, whose entries are $A_{i,j} = 1$ if the inequality (2.1) is satisfied for the node pair (i, j) with $i \neq j$, and $A_{i,j} = 0$ otherwise. For example, in figure 2(*a*), the node $i = 8$ is connected (i.e. $A_{8,j} = 1$) to nodes $j = \{1, 2, 3, 4, 5, 7, 9\}$, as highlighted by the orange links. By definition, visibility networks are connected (i.e. each node i is linked to at least one other node j, e.g. $j = i + 1$ or $j = i - 1$) and undirected (Newman 2018), namely the adjacency matrix is symmetric ($A_{i,j} = A_{j,i}$).

Different from other techniques developed to transform a signal into a network (Zou *et al.* 2018; Iacobello *et al.* 2021), the visibility algorithm does not require any *a priori* parameters. Given a signal, a unique visibility network is obtained in a straightforward way by applying the convexity criterion in (2.1) for each pair of data. Another feature of NVGs is the invariance under affine transformations of the mapped signal, namely translation and rescaling (i.e. multiplication by a positive constant) of both horizontal and vertical axes (Lacasa *et al.* 2008). This implies that two signals with the same temporal (or spatial) structure, but with different mean values (i.e. vertical translation of the series) and standard deviations (i.e. vertical rescaling of the series), are mapped in the same visibility graph.

In the present work, we exploited the NVG approach to study turbulent velocity signals from wall-bounded turbulence, both as a time series (from the boundary layer, § 3.2) and spatial series (from the channel flow, § 3.1). We note that this is the first time the NVG is employed for studying wall-bounded turbulence by focusing on a spatial series rather

than a time series. An optimized code for computing the NVG (either for the spatial or time series) was provided by Iacobello (2020), where the possibility to account for spatial series periodicity is also implemented.

One remarkable feature of NVGs from signals referring to physical phenomena with a wide range of different scales (such as in turbulence) is the infrequent appearance of long-range links. In fact, the presence of fluctuations of different amplitude in the signal prevents the possibility that a node is visible by other distant nodes (Zhuang, Small & Feng 2014). To grasp this concept, the PDF of the link length in $u(x)$ signals from a turbulent channel flow ($Re_\tau \approx 5200$, see § 3.1) is shown in figure 2(*b*), which shows that long-range links are very unlikely to occur (the increasing PDF for large- $\mathcal{L}^+$ values arises from signal periodicity in the x-direction).

The capability of visibility graphs to capture the temporal (or spatial) structure of a signal by means of a convexity-based geometrical framework, hence, turns out to be a key feature to study the occurrence in time (or space) of specific events (Iacobello *et al.* 2018*a*, 2019*a*). In this work, we take advantage from the features of visibility networks to detect FM of the large scales on small scales.

2.2. *Node degree in relation to small-scale signal features*

The degree centrality (or, simply, degree) of a node, i, is defined as the number of neighbours of i, that is, the number of nodes linked to i,

$$k_i \equiv \sum_{j=1}^{N} A_{i,j}, \tag{2.2}$$

where N is the total number of nodes, which corresponds to the number of sampled values of the signal (Newman 2018). The top panel in figure 2(*a*) shows the sequence of degree values for the example of signal, s_i, shown in the bottom of figure 2(*a*); for instance, the degree of node $i = 8$ (highlighted in red) is $k_8 = 7$ because it is connected to seven other points (links are highlighted in orange). By averaging over all nodes, a representative degree value for the network (i.e. for the whole signal) is obtained as $K = \sum_i k_i/N$. It should be noted that the degree, k_i, provides a measure of the extent to which a single node i belongs to a convex interval in the signal, but it is not directly able to quantify whether the properties of node i (e.g. its importance in the network) are similar or not to the properties of other nodes. Instead, this issue can be tackled through assortativity measures, which can be used to assess similarities among nodes (e.g. in terms of their importance in the network through degree–degree correlation) (Newman 2018).

Recalling that long-range links are unlikely to appear in visibility graphs (figure 2*b*), the main contribution to degree values arises from short-range links, which makes the degree a metric that is typically sensitive to the local structure of the signal. Rapidly fluctuating signals are then expected to show lower-degree values, k_i, and in turn, a lower-average degree K (Zhuang *et al.* 2014). Because rapid variations in the local structure of turbulent signals are mainly governed by high frequencies (i.e. low wavelengths), a relation should exist between the average degree, K, and the high-frequency spectral energy (that produces the local variations in the turbulent signals).

With the aim to explore this relation, we report in figure 3(*a*) the energy spectral density of the streamwise velocity, ϕ_{uu}, pre-multiplied for the wavenumber, $\kappa_x = 2\pi/\lambda_x$, from a turbulent channel flow at $Re_\tau \approx 5200$ (see § 3.1). Notice that ϕ_{uu} is normalized by the variance of the streamwise velocity fluctuations, $\langle uu \rangle_{t,x,z}$ (here angular brackets indicate

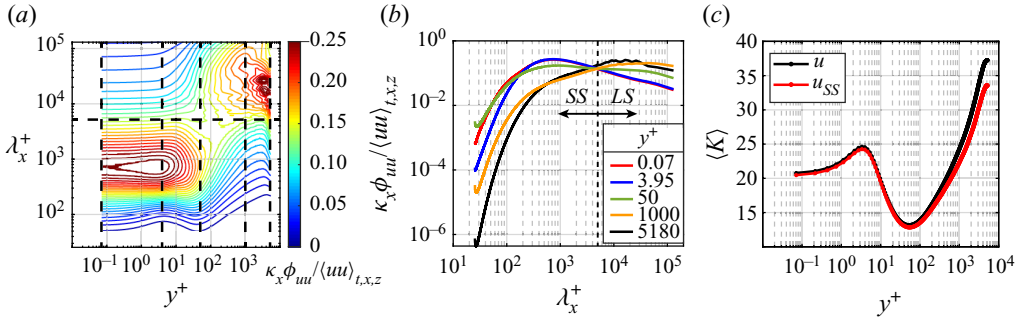

Figure 3. (*a*) Pre-multiplied energy spectral density, ϕ_{uu}, from a turbulent channel flow at $Re_\tau \approx 5200$ (see § 3.1), normalized by the streamwise velocity variance, $\langle uu\rangle_{t,x,z}$. The horizontal dashed line indicates the value of the spectral filter, while vertical dashed lines highlight five representative y^+ coordinates. (*b*) Pre-multiplied energy spectral density for the five selected y^+ locations in (*a*). (*c*) Wall-normal behaviour of the average degree centrality, $\langle K\rangle$, for NVG built from the full streamwise velocity, $u(x_i)$ (black curve), and from the small-scale streamwise velocity, $u_{SS}(x_i)$ (red curve), obtained through a spectral decomposition. Angular brackets in $\langle K\rangle$ indicate averaging over the (homogeneous) spanwise direction, z.

the average over time, t, and homogeneous directions, x, z). In figure 3(*a*), the spectral peak separation is easily distinguishable between the small and large scales, as is the spectral filter adopted in this work, marked by a horizontal dashed line. Five curves of the spectrum at five representative y^+ coordinates (highlighted as dashed vertical lines in figure 3*a*) are also shown in figure 3(*b*).

The rationale behind the normalization of the spectrum through the variance is twofold. First, the streamwise energy density at each y^+ is accentuated, thus emphasizing the occurrence of the two spectral peaks and, second, this normalization permits a congruent comparison with the degree behaviour computed on visibility networks (which are insensitive to different variance levels, i.e. on signal rescaling). Moreover, as a result of the variance normalization, the area under each curve in figure 3(*b*) is equal to unity, so that the integral of curves in figure 3(*b*) in a given range of λ_x represents the fraction of total energy pertaining to that scale range. In this way, figure 3(*b*) elucidates the redistribution of the spectral energy density over scales, λ_x^+, at different y^+ coordinates (a log–log plot in figure 3(*b*) is shown with the aim to highlight the behaviour at small λ_x^+ values).

Focusing on the small scales (that is, $\lambda_x^+ < Re_\tau \approx 5200$) in figure 3(*b*), we observe that by moving from very close to the wall ($y^+ \approx 0.07$) up to $y^+ \approx 4$, there is a small decrease in the (normalized) energy content, then an increase of the (normalized) spectral energy occurs from $y^+ \approx 4$ up to the beginning of the log layer ($y^+ \approx 50$), and lastly a persistent decrease happens up to the channel centreline ($y^+ \approx 5200$). A reduction or a growth of the (normalized) spectral energy at the small scales indicates that the signal tends to be locally smoother (i.e. slowly varying, without rapid low-intensity fluctuations) or more irregular (i.e. rapidly varying), respectively. Recalling that the mean degree, K, is sensitive to the local structure of the signal, an increase of the degree values is then expected for locally smoother signals (i.e. low-spectral energy at local scales) and *vice versa*. Figure 3(*c*) shows the wall-normal behaviour of the mean degree, K, of networks built from the full streamwise velocity, $u(x_i)$ (black line), in the channel flow setup. As expected, the y^+-trend of K for the full signal closely follows the behaviour of the small-scale spectral-energy density as described above, where the degree growth is faithfully related to the small-scale spectral-energy decrease and *vice versa*. In particular, we point out that the value of K at

each y^+ is associated to an integral effect of all wavelengths in the signal, so that $K(y^+)$ arises from a cumulative effect of different spectral-energy levels.

Figure 3(*c*) also shows the y^+-behaviour of the mean degree of networks built from $u_{SS}(x_i)$ (red line), namely, in which the large-scale component is removed. The values and the trends of K from the full and the small-scale velocity signals are very close, and a slight difference appears only very far from the wall. Note that a similar behaviour of K as that shown in figure 3(*c*) for the channel case is also found for the turbulent boundary layer case. It should be noted that because very long-range connections are unlikely to appear (figure 2*b*), they only barely contribute to the average degree, K, which instead is mainly related to shorter links.

The excellent agreement between $K(y^+)$ for the full u signal and the y^+-variations in the small-scale spectral energy (corroborated by the similarity of $K(y^+)$ for u and u_{SS}) indicate that the network degree is able to capture the features of the small-scale turbulence directly from the full signal, i.e. without the arbitrary requirements of filtering operations. These features will be exploited in § 2.3 to provide a metric which is able to quantify FM. We notice that, to the best of our knowledge, this is the first time that insights from the visibility graph approach are directly related to the spectral properties of a signal.

2.3. *FM detection via degree centrality*

The aim of this section is to provide a degree-based metric that is able to quantify FM from full velocity signals. With this aim, in figure 4(*b*), we show a short representative interval of the streamwise velocity series reported in figure 4(*a*), which is extracted from the turbulent channel flow at $y^+ \approx 10$. The corresponding NVG is then built from the short signal in figure 4(*b*), and the links activated by two representative nodes, $i = \{19, 49\}$ (highlighted as red dots in figure 4*b*), are shown as green arcs in figure 4(*c*). Node $i = 19$ clearly displays more connections than node $i = 49$ (i.e. $k_{19} > k_{49}$), because node $i = 19$ is in a larger convex interval than $i = 49$; therefore, the signal around $i = 49$ varies more rapidly than around $i = 19$. Therefore, although the degree, k_i, represents a pointwise value, because k_i refers to a single coordinate i, the information enclosed in k_i originates from the surroundings of i. The degree k_i can then be interpreted as a measure of the instantaneous period (or instantaneous wavelength) at the temporal (or spatial) coordinate t_i (or x_i), by analogy with the concept of instantaneous frequency used in signal analysis (Huang *et al.* 1998; Boashash 2015). Larger k_i values correspond to larger instantaneous periods (or wavelengths), and, in turn, to smaller instantaneous frequencies.

On the basis of this argument and the insights illustrated in § 2.2, we introduce the ratio, K_{np}, to quantify frequency modulation, defined as

$$K_{np} \equiv \frac{K_n}{K_p}, \quad K_n = \frac{1}{N_{neg}} \sum_{j=1}^{N} (k_j \,|\, u_{LS} < 0), \quad K_p = \frac{1}{N_{pos}} \sum_{j=1}^{N} (k_j \,|\, u_{LS} > 0), \quad (2.3a\text{–}c)$$

where K_n and K_p are the average degree values computed on the NVG of the full velocity signal, conditioned to intervals of $u_{LS} < 0$ and $u_{LS} > 0$, respectively, while N_{neg} and N_{pos} are the number of occurrences in which $u_{LS} < 0$ and $u_{LS} > 0$, respectively.

Values of K_{np} greater than 1 indicate that the degree is (on average) larger during $u_{LS} < 0$ intervals than during during $u_{LS} > 0$, and *vice versa* for K_{np} smaller than 1. In the example of figure 4(*b*,*c*), the degree values, k_i, of the two representative nodes in red

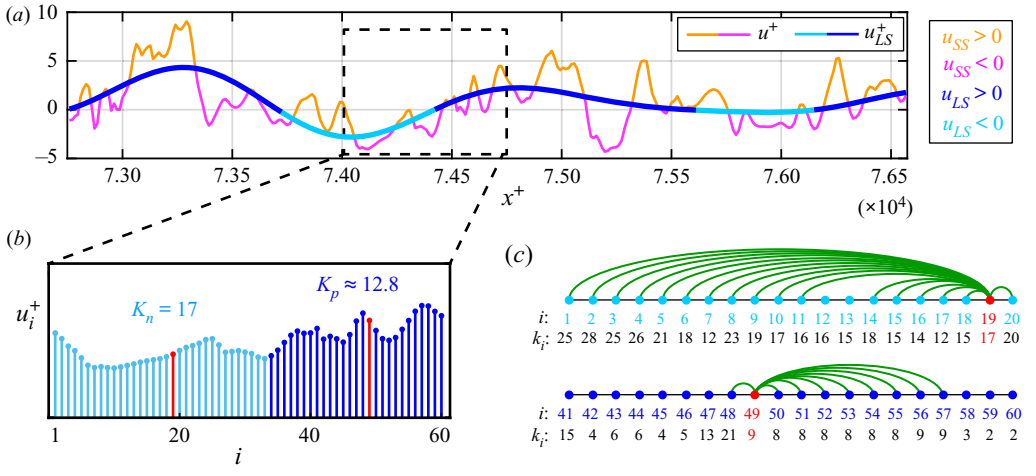

Figure 4. (*a*) An interval of the streamwise velocity, u, and its large-scale component, u_{LS}, extracted along the streamwise direction, x, of the turbulent channel flow at $y^+ \approx 10$. The full u signal is depicted as orange–magenta lines, which indicate intervals of positive and negative small-scale velocity fluctuations, $u_{SS} = u - u_{LS}$, respectively, while the u_{LS} signal is depicted as light–dark blue lines, which highlight intervals of $u_{LS} < 0$ and $u_{LS} > 0$, respectively. Both the series are normalized in wall units. (*b*) A section consisting of 60 data points of the velocity u from (*a*), depicted as vertical bars whose colour reflects the sign of u_{LS}. Two representative data points (corresponding to nodes $i = 19$ and $i = 49$ of the NVG network) are highlighted in red. (*c*) Network representation of the NVG built from the signal in (*b*). Two subsets of nodes and links from the two representative nodes, $i = \{19, 49\}$, are shown as coloured dots and green arcs, respectively. The sequence of degree values, k_i, for each node, i, is also reported.

($k_{19} = 17$ and $k_{49} = 9$) exemplify the behaviour of the two signal intervals during $u_{LS} < 0$ and $u_{LS} > 0$, which result in $K_n = 17$, $K_p \approx 12.8$ and $K_{np} > 1$. Hence, K_{np} discriminates among (i) positive FM for $K_{np} > 1$ (i.e. an increase of the local frequency in the velocity signal gained for $u_{LS} > 0$ and a decrease for $u_{LS} < 0$), (ii) negative FM for $K_{np} < 1$, and (iii) an absence of modulation for $K_{np} \approx 1$. We emphasize that the arguments leading to the ratio (2.3*a–c*) do not involve any *a priori* parameters, but only the unique availability of the full velocity signal to compute the degree value of each node. A filtering operation is only required to condition the degree values to the sign of the large-scale velocity.

To test the NVG-based approach, we built synthetic signals that mimic the near-wall modulation mechanism in wall-bounded turbulence for three modulation cases: amplitude modulation (AM), frequency modulation (FM), and both amplitude and frequency modulation (AM+FM). Appendix A contains details on the synthetic signal construction and reports the K_{np} values for each configuration (see figure 9), which shows that K_{np} is able to highlight the presence of FM and, in presence of both AM and FM mechanisms, tends to be more sensitive to FM while only weakly to AM.

In summary, the K_{np} ratio combines the capability of visibility networks (i) to capture the information on the local temporal structure of a series (§ 2.1), and (ii) to inherit the small-scale energetic features from the full signal (§ 2.2). These characteristics make the visibility approach a powerful and easy-to-use alternative to previously proposed methodologies for time–frequency characterization of turbulence signals. In the following, the NVG approach is carried out for wall-turbulent signals, which reveals its robustness (with respect to different cut-off filtering size) and effectiveness in capturing the large-to-small scale FM mechanism.

3. Description of the turbulent flow datasets

Two main datasets of high-Reynolds-number wall-bounded turbulent flows are exploited in this work to study FM by means of visibility-network-based tools: (i) spatial series from a numerically-simulated turbulent channel flow at $Re_\tau \approx 5200$ (Lee & Moser 2015); and (ii) time series from experimental measurements in a turbulent boundary layer at $Re_\tau = 14\,750$ (Marusic 2020). Although outer flow structures start to occur and play a role in scale interaction at lower Reynolds numbers (Agostini & Leschziner 2014; Hu & Zheng 2018; Wu *et al.* 2019), high-Reynolds-number flows are required to enhance the inter-scale separation and amplify the scale interaction mechanism. Moreover, a third DNS dataset of turbulent channel flow at $Re_\tau = 1000$ is also employed for comparison purposes, thus showing effects of inertia on FM results.

To the best of our knowledge, this is the first time a state-of-the-art DNS at $Re_\tau \approx 5200$ is employed to specifically investigate large-to-small scale FM. In fact, while high-Reynolds-number boundary-layer flows are typically obtained in experimental facilities (as witnessed by most previous works on AM and FM), high-Re_τ experiments of channel flows are difficult to realise owing to strong side-wall boundary effects (Lee & Moser 2015). The DNS employed in this work is at a sufficiently large Reynolds number (i.e. $Re_\tau > 4000$, as reported by Hutchins & Marusic 2007*b*) to guarantee a sufficient large–small-scale spectral separation (e.g. see energy peaks separation in figure 3*a*), and allows us to perform a FM analysis on all the three velocity components that, so far, has only been performed for AM (e.g. see Talluru *et al.* 2014; Agostini & Leschziner 2016).

The scale decomposition of the streamwise velocity fluctuation signals was performed as $u(x) = u_{LS}(x) + u_{SS}(x)$ (e.g. figure 4*a*) and $u(t) = u_{LS}(t) + u_{SS}(t)$ (e.g. figure 1*b*) for the spatial and time series taken from the turbulent channel and boundary layer flows, respectively. A common approach to obtain u_{SS} and u_{LS} is to employ a spectral filter to retain the high and low wavelength or frequency, respectively, as performed in several previous works (Mathis *et al.* 2009*a*; Ganapathisubramani *et al.* 2012; Baars *et al.* 2015, 2017; Pathikonda & Christensen 2017, 2019). Alternatively, Agostini & Leschziner (2014) proposed employing empirical mode decomposition (Huang *et al.* 1998) to separate the large- and small-scale contributions. In this work, both the spectral and empirical mode decompositions were tested to separate the large- and small-scale contributions. However, for the sake of simplicity and in line with most of the current literature, results are only shown for a spectral decomposition, as both the procedures produce equivalent results.

3.1. *DNS of turbulent channel flows*

Velocity fields were extracted from two direct numerical simulations of incompressible turbulent channel flows. The first DNS was run at frictional Reynolds number $Re_\tau \equiv hU_\tau/\nu = 5186$, where $h = 1$ is the half-channel height, $U_\tau = 4.14872 \times 10^{-2} U_b$ and $\nu = 8 \times 10^{-6} U_b h$, with the bulk velocity $U_b = 1$. The size of the spatial domain was $(8\pi h \times 2h \times 3\pi h)$ with $(10\,240 \times 1536 \times 7680)$ grid points along the streamwise, wall-normal and spanwise directions, respectively. The flow fields were recorded only after statistical stationarity of the flow was reached, and 11 temporal frames of the velocity and pressure spatial fields were stored in the dataset. The time interval between two consecutive frames was a flow-through time of approximately 0.7, which corresponded to approximately $3785\nu/U_\tau^2$ in wall units.

The simulation was performed at a sufficiently high Reynolds number and with a sufficiently large spatial domain to exhibit characteristics of high-Reynolds-number turbulence, e.g. the presence of LSMs and a rather large wall-normal range for statistics scaling (Lee & Moser 2015). The dataset is available online (doi:10.7281/T1PV6HJV) from the Johns Hopkins Turbulence Database (Li *et al.* 2008). For further simulation details and statistics, see Lee & Moser (2015).

The second DNS was run at $Re_\tau \equiv hU_\tau/\nu = 1000$, with $h = 1$, $U_\tau = 4.9968 \times 10^{-2}U_b$, $\nu = 5 \times 10^{-5}U_b h$ and $U_b = 1$. The size of the spatial domain was $(8\pi h \times 2h \times 3\pi h)$ with $(2048 \times 512 \times 1536)$ grid points along the streamwise, wall-normal and spanwise directions, respectively. Data were stored for approximately one flow-through time, $[0, 26]h/U_b$, with a storage temporal step of 0.0065. This dataset is also available online (doi:10.7281/T10K26QW) from the Johns Hopkins Turbulence Database (Li *et al.* 2008). For further simulation details, see Graham *et al.* (2016).

In this work, 1-D spatial series (i.e. extracted at a fixed time) of the three velocity components, u, v, w, along the streamwise direction, x, were exploited to build visibility networks. Network-based results were averaged in time (i.e. on 11 temporal frames for the $Re_\tau \approx 5200$ set-up, and on 400 uniformly-spaced temporal frames for the $Re_\tau = 1000$ set-up) and in the spanwise direction; in the latter case, averages were performed for a set of uniformly-spaced spanwise locations separated from each other by 64 and 128 grid points for the $Re_\tau \approx 5200$ and $Re_\tau = 1000$ configurations, respectively.

The cut-off spectral filter to separate the large- and small-scale streamwise velocity for the $Re_\tau \approx 5200$ set-up was set equal to $\lambda_{x,c} = h$ (i.e. $\lambda^+_{x,c} = 5186$), in analogy with previous works in which $\lambda_{x,c}$ was set equal to the boundary layer thickness (Hutchins & Marusic 2007*b*; Mathis *et al.* 2009*a*,*b*; Marusic *et al.* 2010; Dogan *et al.* 2019; Wu *et al.* 2019). For the $Re_\tau = 1000$ set-up, the cut-off filter was $\lambda^+_{x,c} = 5000$, thus was comparable to $\lambda^+_{x,c}$ of the higher-Re_τ channel flow set-up.

3.2. *Experimental turbulent boundary layer at $Re_\tau \approx 14\,750$*

Experimental measurements were performed in the wind-tunnel facility of the University of Melbourne, which employs a 27 m test section, under a free-stream velocity $U_\infty = 19.95$ m s^{-1} (Baars *et al.* 2015). Under these conditions, a zero-pressure-gradient boundary layer developed at a frictional Reynolds number $Re_\tau \equiv \delta U_\tau/\nu = 14\,750$, where $\delta = 0.361$ m is the boundary layer thickness at the measuring location (i.e. 21.65 m from the inlet of the test section), while $U_\tau = 0.626$ m s^{-1} and $\nu = 1.532 \times 10^{-5}$ m^2 s^{-1} at the same streamwise location. The dataset was the same employed by Baars *et al.* (2015, 2017), and is available online at the Fluid Mechanics Research webpage of the University of Melbourne (Marusic 2020).

Time series of the streamwise velocity were simultaneously recorded by means of two constant-temperature hot-wire probes, one at a fixed wall-normal location at $y^+ = 4.33$, and the other vertically moved throughout the boundary layer in the range $y^+ \in [10.5, 2.14 \times 10^4]$ (or $y/\delta \in [7.087 \times 10^{-4}, 1.45]$) for 40 vertical locations. At each wall-normal measurement location, three sets of data were recorded at a sampling frequency of 20 kHz, each one for 120 s corresponding to a large-scale time of $6.6 \times 10^3\delta/U_\infty$, thus ensuring the convergence of spectral statistics at the longest energetic wavelengths (Baars *et al.* 2015). The resulting time step in wall units was $\Delta t^+ = 1.28$. Further details on the measurement procedure and instrumentation can be found in Baars *et al.* (2015).

To separate the large- and small-scale components, we employed a cut-off spectral filter $\lambda_{x,c}^{+} = 7000$ following Hutchins & Marusic (2007*b*), Hutchins (2014) and Baars *et al.* (2015, 2017), who showed this is a proper filter value for turbulent boundary layers at high Reynolds numbers. Differently from the channel flow set-up in which spatial series are considered, here the spectral filter was converted in terms of frequency by invoking the Taylor's hypothesis as $f_c(y^+) = U_c(y^+)/\lambda_{x,c}$, where $U_c(y^+)$ is a local convection velocity at the wall-normal coordinate y^+. The effects of different convection velocities on FM will be elucidated in § 4, where a comparison with spatial data from DNSs is carried out.

4. Results

The results from the application of the degree centrality as a metric to quantify frequency modulation are reported in this section for velocity signals extracted from the turbulent channel flows and the turbulent boundary layer described above. A one-point modulation analysis was carried out: the large scale component, u_{LS}, used to condition the degree on the u_{LS} sign (see (2.3*a–c*)) was extracted at the same y^+ in which the signal was mapped into a visibility network. Owing to the footprint of the LSMs and VLSMs towards the wall, u_{LS} evaluated at each y^+ represented a good estimate of the large-scale velocity component in the outer region, thus resulting in a more applicable procedure than the two-points analysis (Mathis *et al.* 2009*a*). In fact, two-point synchronized measurements are not easy to perform experimentally (Mathis *et al.* 2009*a*). Previous works have shown that similar results are obtained by adopting a one- or two-point procedure for characterizing scales interaction (see, among others, Hutchins & Marusic (2007*a*); Mathis *et al.* (2009*a*); Ganapathisubramani *et al.* (2012)), thus one-point modulation was preferred here for simplicity.

First, the streamwise velocity component, u, was considered, both in an overall perspective (§ 4.1) and with a near-wall focus (§ 4.2). Most of the current literature on scale interaction in wall-bounded turbulence has indeed focused on the u component, being the component in which the large and small scales can be clearly separated. We then extended the analysis to the other velocity components, v and w (§ 4.3). Finally, a space-shifted FM analysis was carried out for all velocity components and for both the turbulence configurations (§ 4.4).

4.1. *FM in the streamwise velocity component*

The values of the ratio K_{np} as a function of the wall-normal coordinate, y^+, are shown in figure 5 for visibility networks built from the streamwise velocity, u. We recall that $K_{np} > 1$ indicates a higher frequency under intervals of positive large-scale velocity than under negative ones, and *vice versa* for $K_{np} < 1$.

Figure 5(*a*) shows K_{np} for the spatial series of the two channel flows DNS at $Re_\tau \approx 5200$ (black) and $Re_\tau = 1000$ (red), while figure 5(*b*) illustrates the K_{np} behaviour for the time series of the boundary layer (green). Values of $K_{np} > 1$ were detected close to the wall for all configurations, while moving away from the wall, K_{np} became smaller than 1, which indicated a reversal in the scale-interaction mechanism, i.e. higher frequencies were detected during $u_{LS} < 0$ than for $u_{LS} > 0$. The overall behaviours shown in figure 5 were in accordance with previous works on scale interaction in wall-bounded turbulence, which have indicated that a higher (amplitude and) frequency of the small scales is found for positive u_{LS} intervals in regions close to the wall, while a reversal mechanism occurs

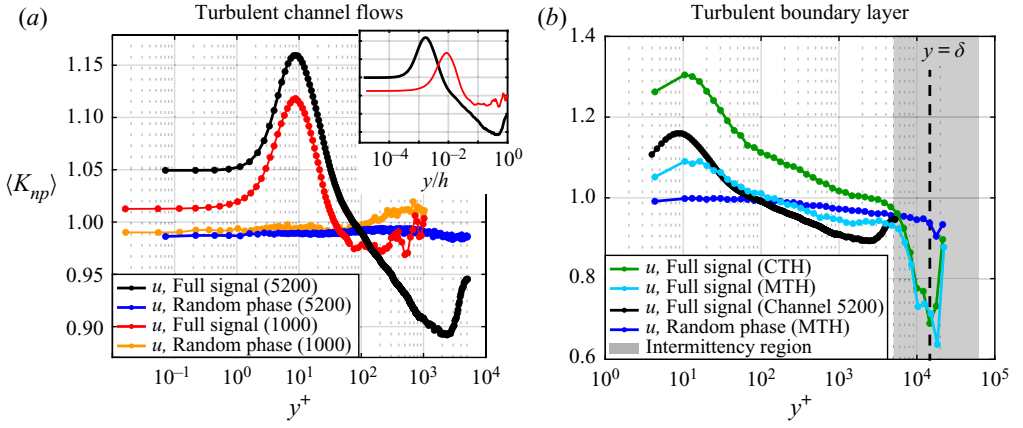

Figure 5. Large-scale conditional average degree ratio, K_{np}, as a function of the wall-normal coordinate, y^+, for streamwise velocity, u, extracted from (a) the channel flow DNS at different Re_τ and (b) the boundary layer experiment. The inset in (a) shows the K_{np} behaviour for the two channel flows as a function of y/h. In (b), $K_{np}(y^+)$ is shown for the spatial series obtained through the classical (CTH) and modified Taylor's hypothesis (MTH) as green and cyan plots, respectively; for comparison, the behaviour for the channel flow at $Re_\tau \approx 5200$ is also reported in black. Moreover, the boundary layer intermittency region is highlighted in (b) as a shaded grey region. Angular brackets indicate averaging over time and spanwise direction in (a) and over three different realizations in (b). The results for synthetic velocity signals with shuffled phases are also shown.

far from the wall (Ganapathisubramani *et al.* 2012; Baars *et al.* 2015, 2017; Pathikonda & Christensen 2017; Awasthi & Anderson 2018; Tang & Jiang 2018; Pathikonda & Christensen 2019). However, the behaviour of $K_{np}(y^+)$ for the two set-ups also highlights peculiar features of large-to-small scale FM that deserve further investigations.

First, we compared the results for the two channel flows at different Reynolds numbers (red and black lines in figure 5a). A similar trend of $K_{np}(y^+)$ was found for both channels, but the intensity of the FM (close to the wall) was larger for $Re_\tau \approx 5200$ than for $Re_\tau = 1000$, thus clearly showing that the effect of higher Reynolds numbers was to increase the FM mechanism in the near-wall region, as a consequence of the increasing magnitude of the large-scale fluctuations with increasing Re_τ. Similarly, away from the wall, the reversal mechanism of scale interaction was strengthened for the higher-Reynolds-number DNS. Furthermore, in figure 5(a) and also in figure 5(b) for the boundary layer, we observed a peak of K_{np} at $y^+ \approx 10$: this peak was shown to be related to strong sweep-like events, a phenomenon referred to as 'splatting' in which the large scales transport the high-intensity small scales towards the wall below the buffer layer (Agostini & Leschziner 2014; Agostini *et al.* 2016). Thus, being the highest small-scale intensity detected in the buffer layer (Agostini *et al.* 2016), the strongest FM is revealed by a peak in K_{np}, which then represents a sensitive metric to local changes in the flow dynamics. Eventually, it was remarkable to observe in figure 5(a) the near-wall agreement of K_{np} plotted against y^+ between the two channel flows at different Reynolds numbers, as the near-wall dynamics is related to near-wall cycle whose characteristic scales are fixed in wall units (see also a discussion on characteristic near-wall spatial and temporal scales in § 4.4).

The behaviour of K_{np} obtained from the time series of the turbulent boundary layer is shown in figure 5(b). When time series are considered, a convection velocity, U_c, has to be defined to apply Taylor's hypothesis in filtering the large and small scales. Typically, U_c is set equal to the local mean velocity, U, and in the following, this assumption will be

referred to as the CTH. Here, K_{np} obtained through the CTH is displayed as a function of y^+ in green in figure 5(*b*); although a similar behaviour with respect to the channel flows is observed (e.g. the black line in figure 5*b*), there is a significant vertical shift when time series are employed. It is worth noting that, because the local mean velocity, U, does not depend on time, the temporal structure of the time series is preserved when the CTH is applied. This implies that the application of any technique (including NVG) to study the scale interaction from a time series is the same as from the corresponding spatial series (i.e. obtained through the CTH), because $\Delta x \propto \Delta t$.

The overestimation of modulation parameters when the time series and CTH are used has been previously observed for AM in jet (Fiscaletti *et al.* 2015), mixing layer (Fiscaletti *et al.* 2016) and turbulent boundary layer flows (Yang & Howland 2018). Specifically, Yang & Howland (2018) reported a distortion of the spatial series when the CTH is used and suggested employing a convection velocity, U_c, defined as $U_c(t) = U + \alpha u(t)$, where $u(t) = u_{LS}(t) + u_{SS}(t)$ is the fluctuating component of the streamwise velocity and $\alpha = O(1)$ is a proportionality constant. The correction proposed by Yang & Howland (2018) is based on the rationale that the sampling time step has to be scaled using the local viscous scales, so that the small-scale activity is enhanced (or reduced) where the wall shear stress is high (or low) owing to an increase (decrease) in the local friction velocity (Yang & Howland 2018). However, variations in the (fluctuating) wall shear stress are mainly induced by variations into large-scale fluctuations, $u_{LS}(t)$, rather than $u(t)$, as observed by Yang & Howland (2018) and reported in the previous literature (e.g. Zhang & Chernyshenko 2016; Baars *et al.* 2017) (see a more detailed discussion about the relation between the near-wall small scales and wall shear stress in § 4.2). Therefore, in this work, we exploited the time varying formulation by Yang & Howland (2018) but only accounted for the large-scale component of $u(t)$, namely

$$U_c(t) = U + \alpha u_{LS}(t). \tag{4.1}$$

In what follows, we will refer to the application of (4.1) as the convection velocity as the MTH, where we selected $\alpha = 0.8$ (which has been proven to be a suitable value). It should be noted that a correction based on u_{LS} arguments was also discussed by Fiscaletti *et al.* (2015) for jet and boundary layer flows to compensate for an AM overestimation. Moreover, it should be noted that, different form the CTH, the structure of $u(x)$ is different from the structure of $u(t)$ for the MTH case, because $U_c(t)$ is not a constant, thus leading to a non-uniform spacing of the spatial series.

The K_{np} behaviour for the MTH is shown in cyan in figure 5(*b*): the overestimation of K_{np} is compensated and its values are much more comparable to the spatial series obtained from DNS of the channel flow at $Re_\tau \approx 5200$ (black line in figure 5*b*). This analysis confirms the applicability of the time-dependent correction of Yang & Howland (2018) for AM when time series are employed, and extends such a correction to the study of FM through (4.1). In particular, we stress that $u_{LS}(t)$ represents a more suitable choice than $u(t)$ in (4.1) because it is assumed that fluctuations in the large-scale velocity, $u_{LS}(t)$, drive the variations in the friction velocity affecting the behaviour of the small scales (see relation (4.2) and the accompanying discussion). In this regard, the relation (4.1) leads to scaling arguments that are in good agreement with the quasi-steady quasi-homogeneous theory, as will be discussed in § 4.2.

One additional feature emerging from figure 5 concerns the reversal in the modulation mechanism from the wall proximity to the outer flow. In fact, while figure 5 shows a continuous decrease of K_{np} for $y^+ > 10$ and $y/h \lesssim 0.5$, an almost absence of FM

was previously found in the log region by means of other techniques (where a reversal of the FM was only detected in the proximity of the end of the boundary layer) (Ganapathisubramani *et al.* 2012; Baars *et al.* 2015). We point out that the K_{np} behaviour in figure 5 resembles the decreasing behaviour of the AM parameters (e.g. see Mathis *et al.* 2009*a*,*b*), with a reversal of K_{np} from the near-wall (where $K_{np} > 1$) towards the outer region (where $K_{np} < 1$). In principle, if the small scales are both amplitude and frequency modulated, one could expect that – following the Newtonian principle that to the same natural effects we must, as far as possible, assign the same causes – a similar underlying mechanism is at play for both AM and FM. This can justify the similarity between the $K_{np}(y^+)$ behaviour, which quantifies FM, and the widely reported behaviour of AM parameters, either in internal or external wall-bounded turbulent flows. Therefore, both AM and FM result from a common underlying phenomenon, for which both the amplitude and frequency of the small scales are concurrently affected by negative or positive large-scale fluctuations at different wall-normal locations.

Specifically, concerning the reversal coordinate (i.e. the y^+ location where K_{np} switches from $K_{np} > 1$ to $K_{np} < 1$), for AM, the reversal typically occurs in the middle of the log region, $y^+ \approx 3.9Re_\tau^{1/2}$ (Mathis *et al.* 2009*a*,*b*; Ganapathisubramani *et al.* 2012; Baars *et al.* 2015). For FM, it is still not clear whether a modulation reversal occurs in the log region (as shown in figure 5) or if it is only limited to the wake region (Baars *et al.* 2015). From figure 5, we can conclude that the FM mechanism is indeed limited to a near-wall region up to approximatively $y^+ = 100$, which is consistent with the analysis by Ganapathisubramani *et al.* (2012). Nevertheless, figure 5 also shows that the reversal y^+ location increases with the Reynolds number. In fact, we find that when the spatial series are focused both from channel DNSs and the time series by the MTH, the reversal coordinates (i.e. $y^+ \approx 35, 75, 145$ for the channel and boundary layer flows at $Re_\tau = 1000, 5186, 14\,750$, respectively) scale as $y^+ \approx 1.15Re_\tau^{1/2}$ (the power-law fit gives an exponent of 0.5 with an $R^2 = 0.985$). This scaling has the same functional relationship found for AM, i.e. $y^+ \approx 3.9Re_\tau^{1/2}$, but with a different proportionality constant. In particular, the $Re_\tau^{1/2}$ trend is reminiscent of the scaling of the outer peak position as a function of Reynolds number (Mathis *et al.* 2009*a*), thus strengthening the underlying connection of FM with the change in large-scale features.

Another notable aspect discernible in figure 5 is the V-like shape of K_{np} in the outer region of the channel flow, i.e. around $y/h \approx 0.5$ ($y^+ \approx 2500$). In the literature, the increase, which gives the V-like shape, of AM of the small scales (which are representative of fine-scale turbulent motion) can be observed close to the channel centre, e.g. in Chung & McKeon (2010) (see figure 4 therein) for the streamwise velocity, u, or in Yao *et al.* (2018) (see figure 3(*c*) therein) for the v and w components. However, to the best of our knowledge, this peculiar increase of the modulation parameter in the channel flow has not been explicitly discussed so far. Here we propose an interpretation based on the insights gained from turbulent boundary layers.

Previous analyses, in fact, have highlighted that the preferential arrangement of the small scales in the wake region of turbulent boundary layers is mainly affected by intermittency, namely the presence of bulges of turbulent and non-turbulent flow (Baars *et al.* 2015, 2017). However, figure 5(*a*) shows a similar V-like behaviour – as for previous results on AM – also in the outer region of the channel flows, despite the absence of a turbulent/non-turbulent region in the channel flow (that is, an internal flow). In particular, the V-like shape for the channel at $Re_\tau = 1000$, although less evident than at $Re_\tau \approx 5200$, consistently occurs at $y/h \approx 0.5$, as highlighted in the inset of figure 5(*a*).

Here we suggest that, similar to the effect of intermittency in boundary layer flows, the preferential arrangement in the proximity of the channel centreline could be affected by an alternating occurrence of high- and low-rotational fluid motion above the head of large- or very-large-scale structures. This phenomenon would lead to the increase of both the AM and FM parameters toward the channel centreline. Although the clarification of this issue goes beyond the aim of this work, we do believe it deserves future investigations, as the channel flow set-up is much less considered for scale interaction analyses than the turbulent boundary layers (for which high Re_τ data are much more readily available from experimental measurements).

With the aim to ensure that the behaviour of $K_{np}(y^+)$ described so far is the result of an intrinsic flow phenomenon, rather than an artefact arising from the network representation, figure 5 shows the results for random-phase signals. Through a randomization of the phase of velocity Fourier coefficients, the energy spectral density and the turbulence intensity do not change, but all phase information is lost. Hence, following Mathis *et al.* (2009*a*), first the signals of u were phase-scrambled, then the large-scale component, u_{LS}, was extracted from the new random-phase signal (the amplitude spectrum was not changed), and eventually the degree was calculated from the full random-phase signal and conditioned to the sign of the random-phase u_{LS}. Figure 5 shows that in both the channel flow and boundary layer set-ups, the characteristic behaviour of K_{np} for turbulent signals (black curves) disappeared for the random-phase velocity signals (blue curves). As previously reported (e.g. see Chung & McKeon 2010), phase relationships between the large and small scales play an important role in the characterization of scale interaction, specifically on scale modulation; thus, if any realistic phase information is lost, modulation effects will disappear as well.

The NVG-based approach is demonstrated to be reliable in capturing FM in turbulent velocity signals, and sensitive to phase randomization. Moreover, the behaviour of $K_{np}(y^+)$ for both the channel and boundary layer is found to be robust under different cut-off wavelengths (used to extract u_{LS} from the full signal u), as discussed in Appendix B. Further insights into the FM of the streamwise velocity will be presented in § 4.2 focusing on the near-wall region, i.e. where large-to-small scale modulation essentially takes place.

4.2. *Scale interaction in the near-wall region*

The presence of a near-wall modulation, whose intensity increases with the Reynolds number, has posed a challenge to the classical view on the universality of near-wall turbulence, i.e. the independence of the near-wall statistics (scaled in wall units) to the Reynolds number when this is sufficiently large. Because large-scale structures affect the behaviour of the wall shear stress (Mathis *et al.* 2013), the classical universality hypothesis has been recently replaced with the hypothesis that statistics have to be normalized by considering the large-scale skin friction, τ_{LS}, rather than the mean skin friction, τ_w (Zhang & Chernyshenko 2016; Chernyshenko 2020). This hypothesis is referred to as the quasi-steady quasi-homogeneous (QSQH) hypothesis, because the temporal and spatial variations of the large-scale structures are much slower than variations of the near-wall turbulence (Zhang & Chernyshenko 2016).

The aim of this section is (i) to provide the proportionality relationships between u_{LS} and the (temporal or spatial) frequency of the small scales as expected from the QSQH hypothesis; and (ii) to test the validity of such relationships by means of the network

degree centrality. In particular, we will focus on velocity signals extracted at $y^+ = 15$, which corresponds to the y^+ value of maximum K_{np} in figure 5, thus being a representative wall-normal coordinate of the near-wall region. This choice is also related to the fact that, evidenced by Zhang & Chernyshenko (2016) and Agostini & Leschziner (2019), the validity of the QSQH hypothesis is found to be rather accurate only in a narrow region close to the wall, that is, $y^+ < 70 - 80$.

According to the QSQH hypothesis, variations in the large-scale velocity, u_{LS}, induce proportional variations in the large-scale skin friction, τ_{LS}, namely $(\tau_w + \tau_{LS}) \propto (U + u_{LS})$, where U is the local mean velocity. Because, by definition, $U_\tau = \sqrt{\tau_w/\rho}$ (where ρ is the fluid density), the effect of u_{LS} on τ_{LS} can be stated in terms of velocities as

$$(U_\tau + u_{\tau,LS}) \propto \sqrt{(\tau_w + \tau_{LS})} \propto \sqrt{(U + u_{LS})}, \tag{4.2}$$

where $u_{\tau,LS}$ is the fluctuating (i.e. zero-mean) large-scale component of the friction velocity (Baars *et al.* 2017). Owing to near-wall modulation, a quasi-steady or quasi-homogeneous variation of the friction velocity affects also the (amplitude and) frequency of the small scales. Specifically, $u_{LS} > 0$ events induce $u_{\tau,LS} > 0$ (see relation (4.2)) that, in turn, produces an increase of the small-scale instantaneous spatial or temporal frequency according to the FM mechanism; and *vice versa* for $u_{LS} < 0$ (Baars *et al.* 2017).

In the near-wall region, the spatial scales are supposed to have a constant characteristic length when normalized in wall units (e.g. see the inner spectral peak for $\lambda_x^+ = \lambda_x U_\tau/\nu = \text{const.} \approx 1000$ in figure 3*a*). Therefore, spatial scales are related to $u_{\tau,LS}$ variations as $\lambda_x(U_\tau + u_{\tau,LS}) = \text{const.}$, namely $\lambda_x \propto 1/(U_\tau + u_{\tau,LS})$. Because the spatial frequency (i.e. wavenumber), κ_x, is related to the spatial scales as $\kappa_x \propto \lambda_x^{-1}$, by using (4.2), we obtain the following scaling relations:

$$\lambda_x \propto (U + u_{LS})^{-1/2}, \quad \kappa_x \propto (U + u_{LS})^{1/2}. \tag{4.3a,b}$$

In the case of a time series, the temporal frequency, f, is related to the spatial scales as $f = U_c/\lambda_x$, where U_c is the convection velocity. Assuming that U_c scales in wall units (Baars *et al.* 2017), namely $U_c \propto (U_\tau + u_{\tau,LS})$, the temporal frequency is eventually expected to scale as

$$f \propto (U_\tau + u_{\tau,LS})^2 \propto (U + u_{LS}). \tag{4.4}$$

Therefore, the relations (4.3*a*,*b*) and (4.4) represent the expected scaling of the spatial and temporal frequency, respectively, according to the QSQH hypothesis.

As discussed in § 2.3, the degree centrality represents a measure of the instantaneous wavelength or a temporal period. Therefore, it is expected that the degree, k, scales as $k \propto \lambda_x$ for the channel flow (in which spatial series are mapped into NVGs), and $k \propto 1/f$ for the boundary layer (in which time series are analysed). If the degree is indeed an effective parameter to quantify FM, k should then be proportional to $(U + u_{LS})^{\beta_{u,x}}$ in the channel flow and $(U + u_{LS})^{\beta_{u,f}}$ in the boundary layer. Following the aforementioned scaling arguments (i.e. relations (4.3*a*,*b*) and (4.4)), the two exponents that verify the QSQH hypothesis should be equal to $\beta_{u,x} = -0.5$ and $\beta_{u,f} = -1$.

To test the $\beta_{u,x}$ and $\beta_{u,f}$ scaling, we conditionally averaged the degree centrality values (computed from NVGs of the full velocity signals $u(x)$) to the u_{LS} values at $y^+ \approx 10$. In particular, the u_{LS} values were first divided into uniformly-binned intervals in the range between $min[u_{LS}]$ and $max[u_{LS}]$. Then, for each visibility network (i.e. each signal), nodes i, for which $u_{LS}(i)$ belongs to a specific bin, were selected, and the corresponding degree

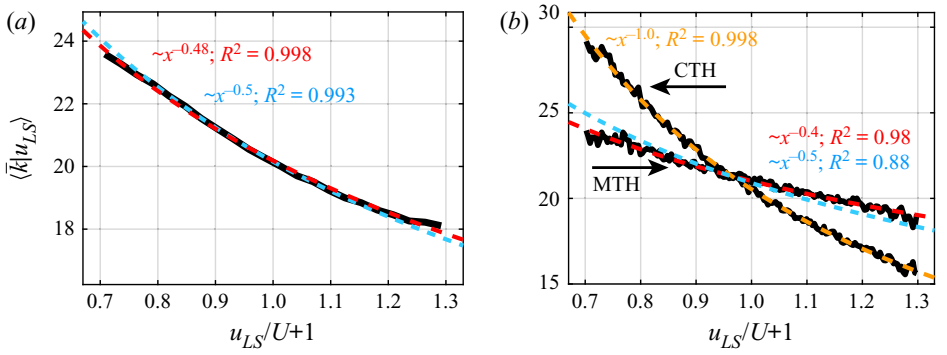

Figure 6. Average degree conditioned to the u_{LS} values as a function of the normalized u_{LS} deviation, for u signals at $y^+ \approx 10$ in (*a*) the turbulent channel flow and (*b*) the turbulent boundary layer (angular brackets indicate the average over time and homogeneous directions). In (*b*), the scaling for the spatial series obtained through the CTH and MTH are shown as black lines. The power-law fitting curves are shown as dashed lines, together with the exponent of the fitting and the coefficient of determination, R^2, for both set-ups. Light-blue dashed lines correspond to the expected scaling trends for the spatial data. The intervals of $u_{LS}/U + 1$ in abscissa cover, for each set-up, a range from the 5th to the 95th percentile of all u_{LS} at the selected vertical coordinate $y^+ \approx 10$.

values, k_i, were averaged for that specific bin. By extending the averages to all u_{LS} bins, the conditional average, $(\bar{k} \,|\, u_{LS})$, was obtained, where the overbar indicates an average over a set of nodes. When plotting $(\bar{k} \,|\, u_{LS})$, the u_{LS} value representative of each bin was chosen as the middle value of the bin.

The behaviour of $(\bar{k} \,|\, u_{LS})$ as a function of u_{LS} revealed the scaling between degree-based frequency variations and large-scale velocity variations. Such conditional degree averages are shown in figure 6 for the channel flow at $Re_\tau \approx 5200$ (figure 6*a*) and the boundary layer (figure 6*b*), as a function of $(u_{LS}/U + 1)$, where $U = U(y^+ = 10)$ is constant and $(u_{LS}/U + 1)$ values equal to 1 correspond to large-scale zero-crossing points ($u_{LS} = 0$). We find a scaling of the conditioned degree, which follows a power-law with the best-fit exponent $\beta_{u,x} = -0.48$ for the channel flow (spatial data) and $\beta_{u,f} = -1$ for the boundary layer when the local mean velocity is used in the Taylor's hypothesis (CTH). These exponent values are in excellent agreement with the expected values of -0.5 and -1. We recall that, for the CTH case, because the convection velocity is constant and equal to the local mean velocity U, the scaling exponent obtained is representative of a (temporal) frequency, thus $\beta_{u,f} = -1$. However, when the MTH is employed (4.1), the structure of the spatial series (obtained from the corresponding time series) significantly changes and scaling arguments are therefore congruent with the DNS spatial series. Accordingly, the $(\bar{k} \,|\, u_{LS})$ scaling for the MTH case in figure 6(*b*) produces an exponent which is close to -0.5, as expected from the spatial series. Finally, we mention that an exponent $\beta_{u,x} = -0.5$ is found for the channel flow at $Re_\tau = 1000$ with an $R^2 \approx 0.92$ when the cut-off filter is set to $\lambda^+_{x,c} = 2500$, while for larger $\lambda^+_{x,c}$ values, a poorer fitting is observed, likely as a result of the limited scale separation for this set-up.

The conditional averages were performed here by using uniformly-binned intervals of u_{LS}, whereas Baars *et al.* (2017), by adopting a variable-interval scheme for conditional averages, reported a scaling of approximatively 0.8 (instead of 1) for the frequency in turbulent boundary layers over a wide range of Re_τ. They indicated that the discrepancy in the expected exponent might be caused by an inaccurate assumption that the small scales are convected at a fixed inner-scaled velocity. However, here we show that the expected

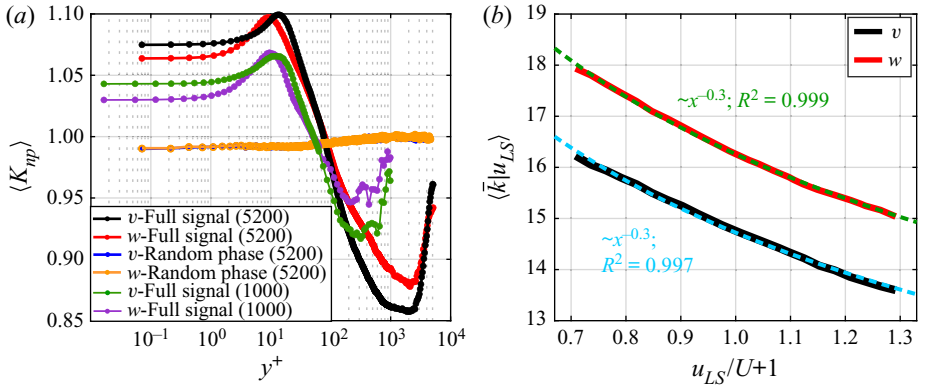

Figure 7. (*a*) The K_{np} ratio as a function y^+ for the wall-normal and spanwise velocity components, v and w, extracted from the two channel-flow DNSs, together with the corresponding K_{np} values for random-phase signals. The respective Reynolds number value of the DNS is reported within brackets in the legend. Angular brackets indicate averaging over time and the spanwise direction. (*b*) Average degree conditioned to the u_{LS} values as a function of the normalized u_{LS} deviation for v and w signals at $y^+ \approx 10$ in the turbulent channel flow at $Re_\tau \approx 5200$. The power-law fitting curves are shown as cyan and green dashed lines for the v and w cases, respectively, together with the exponents of the fitting and the coefficients of determination, R^2.

scaling for f is still obtained by assuming $U_c \propto (U_\tau + u_{\tau,LS})$, which suggests that the discrepancy in the fitting in Baars *et al.* (2017) might be related to different methodological arguments.

The relevance of the scaling shown in figure 6 is twofold. First, it demonstrates that, similarly to the near-wall AM (Baars *et al.* 2017), the near-wall FM agrees with the quasi-steady quasi-homogeneous hypothesis. Second, the outcomes of figure 6 further validate the capability of the visibility-based approach, which relies on the degree centrality, to capture FM in wall-bounded turbulence, as well as the validity of the MTH (4.1) in converting a time series into a spatial series.

4.3. *Analysis of the spanwise and wall-normal velocity components*

The application of the NVG approach to the spatial series of wall-normal, $v(x)$, and spanwise, $w(x)$, velocity from the DNS of the turbulent channel flows is here reported. Figure 7(*a*) shows the ratio K_{np} for the v (black and green curves) and w (red and purple curves) components as a function of y^+ for the two channel flows at different Re_τ. Here, $K_{np} > 1$ is found in the near-wall region, which indicates a positive frequency modulation of the large scales on the small scales of v and w. This result is consistent with the AM investigations, which show a similar modulating effect of the large scales on the small scales of the three velocity components (Hutchins & Marusic 2007*b*; Talluru *et al.* 2014; Yao *et al.* 2018; Wu *et al.* 2019). In particular, the trends shown in figure 7(*a*) are similar to that reported in figure 5(*a*) for the u signals, although lower K_{np} values are obtained from v and w. Moreover, as for u, the FM of the small scales of v and w is weaker at lower Reynolds number, because smaller K_{np} values are observed in the near-wall region for $Re_\tau = 1000$.

Furthermore, similar to the u component, an almost constant $K_{np} \approx 1$ behaviour is found for the network built from the random-phase v and w signals (see orange and blue curves in figure 7(*a*) referring to $Re_\tau \approx 5200$ as a representative case), which confirms the ability of

the degree to capture phase information from the (full) signal. It should be noted that, for the sake of consistency, a unique phase shuffling was performed in this case for the three velocity components. As the degree centrality from the v and w signals is conditionally averaged on u_{LS}, the phase of the streamwise velocity signal was extracted and randomly shuffled, so that the random-phase u_{LS}, v and w signals were obtained via the respective (non-shuffled) amplitudes but with the same random phases.

Although spectral peak separation in the spectrograms of the transversal velocity components is less evident than for the streamwise velocity, the generation and amplification of small-scale motions (i.e. fine-scale vortices) of all the three velocity components are strongly connected with large-scale events (Hutchins & Marusic 2007*b*). Within this perspective, the wall-normal and spanwise velocities are expected to be modulated in the near-wall region by following the QSQH hypothesis in a similar way as the streamwise component, u. However, while results for AM of the three velocity components (Talluru *et al.* 2014; Agostini & Leschziner 2019; Chernyshenko 2020) and scaling arguments for the AM and FM of the u component (Baars *et al.* 2017) have been provided, as far as we know, similar scaling arguments (as in Baars *et al.* (2017), figure 9 therein) for v and w have not been pursued for FM to date.

By analogy with the modulation of the u component, the conditional average degree, $(\bar{k}\,|\,u_{LS})$, is evaluated as a function of $(u_{LS}/U+1)$ at $y^+ \approx 10$ for NVGs built from $v(x)$ and $w(x)$ signals. The conditional average degree and the corresponding fitting are shown in figure 7(*b*) for the $Re_\tau \approx 5200$ set-up and confirm the power-law modulation effect of the large scales in the near-wall region even for the other velocity components, namely $k \propto (U+u_{LS})^{\beta_{v,x}}$ and $k \propto (U+u_{LS})^{\beta_{w,x}}$. However, while, for the u component, the exponent of the power-law was $\beta_{u,x} \approx -0.5$, a weaker scale interaction effect was found for the v and w components, being $\beta_{v,x} \approx -0.3$ and $\beta_{w,x} \approx -0.3$, which are both smaller (in modulus) than $\beta_{u,x}$. This outcome is consistent with the smaller K_{np} values for v and w (see figure 7*a*) than for u (see figure 5*a*), which indicates a weaker FM in the near-wall region for the transversal velocity components.

The power-law relationships found for u, v and w suggest that, although the intensity of modulation is different for each velocity component, the response of the small-scales of v and w exhibits a functional relation qualitatively analogous to the response of u. In general, there could be several factors playing a role in the scale-interaction mechanisms (such as the direction of the large scales as discussed by Chernyshenko 2020), but we can conclude that the QSQH hypothesis is valid for all velocity components, although a more refined description is required for the transversal components, v and w.

The results shown in this section reveal that the three velocity components are all affected by a large-scale FM in the near-wall region, where an increase of the local (spatial) frequency is observed under $u_{\tau,LS} > 0$ periods induced by positive u_{LS} events. In particular, we provide novel insights on FM for the v and w components, which have been investigated less than u, in terms of FM intensity for the spatial series (figure 7*a*) and scaling arguments on the QSQH hypothesis (figure 7*b*).

4.4. *Time and space shifting in FM*

To conclude our analysis, we provide results on the investigation of the time- and space-shifted FM, as quantified by K_{np}. We recall that a lead of the small-scale amplitude was found with respect to the large scales in the near-wall region of turbulent boundary layers, while a small-scale lag is found above the reversal coordinate (Bandyopadhyay & Hussain 1984; Guala *et al.* 2011). Concerning FM, a lead of the small-scale frequency

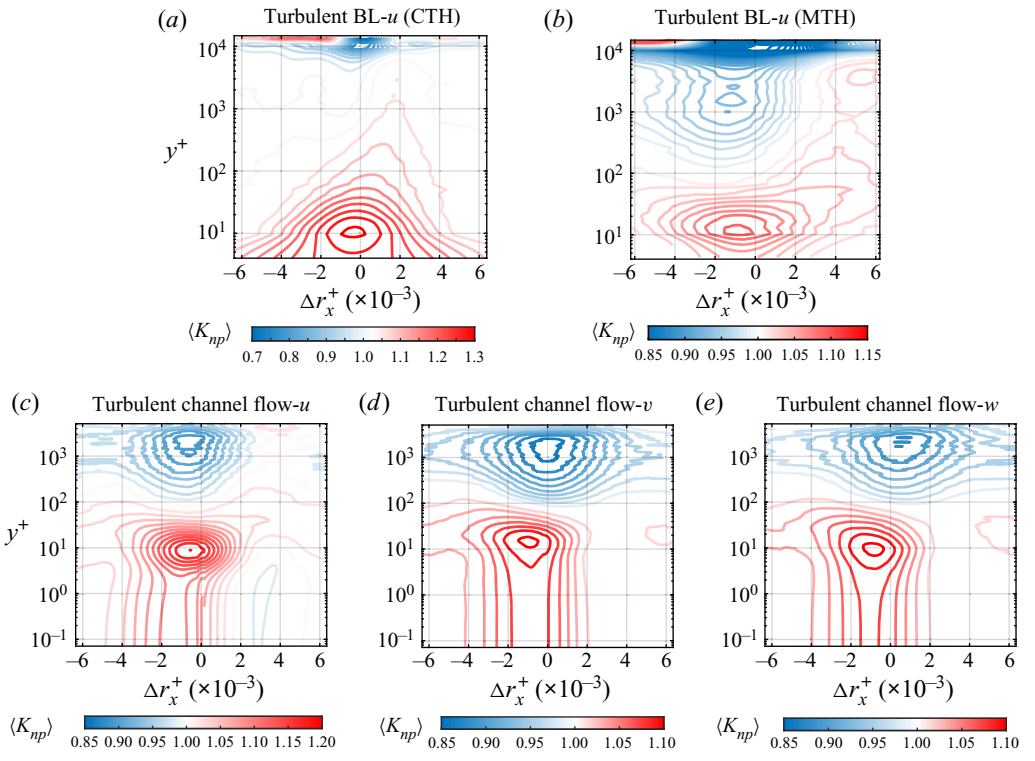

Figure 8. Contour plot of the K_{np} ratio as a function of the wall-normal coordinate, y^+, and the temporal or spatial shifting, Δt^+ or Δr_x^+, respectively. Shiftings for the turbulent boundary layer are reported in (*a*,*b*) whether the CTH or MTH is used, respectively. The spatial shifting for the turbulent channel flow at $Re_\tau \approx 5200$ is shown in (*c*–*e*) for the three velocity components. Iso-level contours are displayed by using a level-step equal to 0.03 in (*a*), 0.01 in (*b*) and 0.015 in (*c*–*e*).

with respect to the large scales was found in the near-wall region but, different from AM, scattered behaviours were found far from the wall (Ganapathisubramani *et al.* 2012; Baars *et al.* 2015).

To address this issue, in figure 8, we show the conditionally average degree, K_{np}, as a function of y^+ and the spatial delay, Δr_x^+, where for the time series, it holds the Taylor's hypothesis $\Delta r_x^+ = -U_c \Delta t^+$ (the minus sign highlights the opposite direction of the reference systems between the fixed-point time series and spatial series). Therefore, the formulation of K_{np} reported in (2.3*a*–*c*) is extended to account for spatial shifting, Δr_x^+, as $K_{np}(\Delta r_x) = K_n(\Delta r_x)/K_p(\Delta r_x)$, with

$$\left.\begin{aligned} K_n(\Delta r_x) &= \frac{1}{N_{neg}(\Delta r_x)} \sum_{j=1}^{N} \big(k(x_j - \Delta r_x) | u_{LS}(x_j) < 0\big), \\ K_p(\Delta r_x) &= \frac{1}{N_{pos}(\Delta r_x)} \sum_{j=1}^{N} \big(k(x_j - \Delta r_x) | u_{LS}(x_j) > 0\big). \end{aligned}\right\} \tag{4.5}$$

Positive or negative Δr_x^+ values indicate in (4.5) a lag or lead, respectively, of the degree, k, with respect to u_{LS} in the conditional averages of (2.3*a*–*c*) (the results in figure 5 correspond to $\Delta r_x^+ = \Delta t^+ = 0$). If the CTH is employed for the turbulent boundary layer

time series (figure 8*a*), a slight lead of K_{np} with respect to u_{LS} (i.e. high K_{np} values are at $\Delta r_x^+ < 0$ but close to $\Delta r_x^+ = 0$) is observed for $y^+ \lesssim 15$. However, a more substantial lead is observed for larger y^+ coordinates in the near-wall region up to $y^+ \approx 100$, in agreement with previous analyses (Baars *et al.* 2015), while a lag of K_{np} with respect to large scales is detected for $y^+ \gtrsim 100$. A clearer picture is obtained when the MTH is exploited (figure 8*b*). Significant lead of K_{np} with respect to u_{LS} is found in the whole near-wall region (including the wall proximity, $y^+ \lesssim 15$), while the lag for $y^+ \gtrsim 100$ is less evident and a lead is recovered for larger y^+ values (see blue contours in figure 8*b*). Eventually, no clear patterns are observed in the intermittent regions ($y^+ \gtrsim 5 \times 10^3$).

The space-shifted K_{np} values in the turbulent channel flow at $Re_\tau \approx 5200$ for the three velocity components are displayed in figure 8(*c–e*). Similar to the turbulent boundary layer, a lead of K_{np} with respect to u_{LS} is found for $y^+ < 100$, as highlighted by high K_{np} values for $\Delta r_x^+ < 0$. Differences among the u, v and w components are detected in proximity of the channel centreline, where K_{np} appears to lead, be in-phase and slightly lag u_{LS} for the u (figure 8*c*), v (figure 8*d*), and w components (figure 8*e*), respectively. It should be noted that the $Re_\tau \approx 5200$ is here used as a representative set-up for spatial data, and the results for the lower Re_τ channel flow are in agreement with the results in figure 8, so they are not shown for the sake of conciseness.

In particular, it is worth highlighting that the maximum K_{np} values in the near-wall region are found at $\Delta r_x^+ \approx 1000$ for the streamwise velocity in the turbulent boundary layer when the MTH is employed (figure 8*b*), as well as for all the velocity components in the turbulent channel flow (figure 8*c–e*). The value $\Delta r_x^+ \approx 1000$ is in excellent agreement with the characteristic length scale in the near-wall region, being $\lambda_x^+ = O(10^3)$ (see inner spectral peak in figure 3*a*). The equivalent time scale is $\Delta t^+ = \Delta r_x^+ / U_c^+ \approx 100$ (being $U_c^+ \approx 10$ in the buffer layer and viscous sublayer), which is the characteristic turnover time of the near-wall cycle. As the small scales are supposed to be actively modulated by the large scales, the time taken for this process to be completed is therefore equivalent to the time scale of the near-wall cycle (Ganapathisubramani *et al.* 2012).

The results shown in figure 8(*a–c*) for the streamwise velocity reveal that different convection velocities indeed play a significant role in the FM dynamics, not only in terms of overestimation (as highlighted in figure 5*b*), but also in terms of spatial delay that, in the near-wall region, is strongly related to the near-wall cycle. Therefore, NVG is again revealed to be a reliable approach for quantifying FM even in the presence of a temporal or spatial shifting. Finally, we note that an important issue about scale interaction is whether the large scales actually cause an increase or decrease of the small-scale activity, as the parameters used so far to quantify AM and FM only show that there is a relation (e.g. a correlation) between the large scales and small scales. Although definite answers to this issue are not still available, our detection of the presence of a significant temporal or spatial delay close to the characteristic time or length scale of the near-wall cycle, in conjunction with the arguments leading to relation (4.2), could provide supporting clues that a causation process is at play. In fact, fluctuations in the large-scale component of the wall shear stress, which affect the small-scale behaviour, appear to be directly caused by the outer large-scale structures rather than being the feature of near-wall processes (Zhang & Chernyshenko 2016).

5. Discussion

In this work, the natural visibility graph was used to study the 1-D spatial series and time series from two turbulent flow configurations, but some generalizations can be outlined.

First, the geometrical criterion at the basis of the visibility algorithm can be extended to scalar fields of arbitrary dimension (Lacasa & Iacovacci 2017). For instance, Tokami *et al.* (2020) recently constructed a spatial visibility graph (employing a simplified version of the NVG, horizontal visibility graph, as proposed by Luque *et al.* 2009) from a 2-D velocity field in a buoyancy-driven turbulent fire. Therefore, our approach could be extended to 2-D velocity fields at fixed y^+ coordinates, thus concurrently taking into account the degree variations along the streamwise and spanwise directions.

The results provided by natural visibility graphs, specifically about the degree centrality, necessarily depend on the signal resolution (either the sampling frequency or the grid size), which needs to be sufficiently high to capture the behaviour of the small scales. However, if the temporal or spatial resolution is sufficient to capture the smallest significant features of the signal, the degree centrality tends to proportionally scale with the signal resolution, as has already been shown, e.g. in Iacobello *et al.* (2018*b*). Nevertheless, an additional feature of visibility networks is the possibility to explicitly account for the spatial or temporal discretization. In fact, one can assign to each discrete observation, i, the corresponding signal spacing (e.g. Δx_i, Δz_i, Δt_i, etc.). In this way, each node i of the network is representative of an interval centred in i, thus providing a continuous representation of the signal. As a result, a weighted network is obtained in which the relation (2.2) is reformulated as $\tilde{k}_i \equiv \sum_j \Delta\chi_j A_{i,j}$ for a series sampling, $\Delta\chi_j$, where χ is independent variable (e.g. time). This generalization is particularly useful for non-uniformly sampled signals from experimental measurements, in which $\tilde{k}$ can be used in place of k, e.g. in the definition (2.3*a–c*).

Finally, it is worth observing that, so far, the visibility approach has been presented as a convexity criterion (see inequality (2.1)). In particular, the network degree was interpreted as a measure of the instantaneous period (quantified in terms of the local convexity of the signal), in analogy with the concept of instantaneous frequency based on the Hilbert transform (where the local properties of a series are emphasized by performing a convolution of the signal with the function $1/t$ (Huang *et al.* 1998)). Nevertheless, the visibility algorithm can also be used as a concavity criterion by applying it to the opposite signal, $-s_i$, whose effect is to change the direction in the inequality (2.1) (Iacobello *et al.* 2019*a*). The comparison of the network metrics extracted from s_i and $-s_i$ allows the characterization of the peak–pit asymmetry of a signal, especially in real-world phenomena (Hasson *et al.* 2018). Following this point of view, we evaluated, for the sake of completeness, the values of $K_{np}(y^+)$ by using the NVG as a concavity criterion for the streamwise velocity, and we found that the main features of the FM for full and random-phase signals are retained when the information is only taken from either the convexity or concavity criterion.

6. Conclusions

In this study, we propose a novel approach to investigate the frequency modulation (FM) mechanism in wall-bounded turbulence by means of the natural visibility graphs. The spatial series and time series of the velocity from two turbulent channel flows and a turbulent boundary layer, respectively, are mapped into visibility networks and the degree centrality is conditionally averaged to the sign of the large-scale velocity to quantify FM. In particular, the versatility of visibility graphs to map either the time or spatial series, allows us to exploit the velocity spatial fields from turbulent channel flows that have been much less investigated than turbulent boundary layers under the lens of FM.

The overall results for the streamwise velocity indicate a FM mechanism occurring in the near-wall region with a peak of intensity in the buffer layer, in agreement with previous works. However, in contrast with the previous observations on FM, we observe a reversal in the FM mechanism far from the wall, similar to what is observed for AM, in both channel and boundary layer flows. We propose that such similarity could stem from a common underlying phenomenon, for which both the amplitude and frequency of the small scales are concurrently affected by negative or positive large-scale fluctuations. Moreover, we observe that the reversal coordinate scales as $Re_\tau{}^{0.5}$, which is reminiscent of the scaling in the wall-normal position of the outer spectral peak.

The effect of different convection velocities for the time series analysis is also discussed. In particular, we modify the correction proposed by Yang & Howland (2018) by accounting for only the large-scale velocity component in the definition of the convection velocity. This choice is based on the rationale that variations in the large-scale velocity induce variations in the wall shear stress, which, in turn, affect the behaviour of the small scales. We detect an overprediction of the FM when the local mean velocity is employed as the convection velocity in the turbulent boundary layer, while such overprediction is compensated when the proposed MTH is used. Moreover, scaling behaviours of the degree centrality as a function of the large-scale velocity are found to be in excellent agreement with the the QSQH theory. In this regard, our correction of the Taylor's hypothesis provides reliable scaling trends as the large-scale velocity is supposed to induce a modulation of the small scales through variations in the wall shear stress.

Finally, the FM for the wall-normal and spanwise velocity components is analysed for the turbulent channel flows and FM scaling is discussed for the transversal velocities. We find a FM mechanism for the wall-normal and spanwise velocity components qualitatively similar to FM of the streamwise velocity. Specifically, a power-law scaling of the degree conditioned to the large-scale velocity is found for the three velocity components, although smaller exponents are found for the transversal velocities than for the streamwise velocity. Moreover, a delay-based analysis is carried out for the three velocity components in the channel flow and for streamwise velocity time series in the boundary layer. We observe that the small scales lead the large scales in the near-wall region (in accordance with previous studies), but significant differences are found when the CTH or MTH is applied. Specifically, our MTH provides results in agreement with spatial series analysis, where the delay of maximum modulation corresponds to the characteristic length (or temporal) scale of the near-wall cycle.

Furthermore, we emphasize here that, to the best of our knowledge, this is the first time that FM is thoroughly investigated for all the three velocity components, as previous works have mainly focused on AM. The findings gained through the visibility networks of all the three velocities can then contribute to the development of a more general model of scale interaction, which accounts for the different modulating effect of the large scale on each velocity component.

The visibility-based approach reveals to be robust in the quantification of FM with respect to AM (Appendix A), and to different cut-off filtering sizes and high-frequency noise (Appendix B), as well as sensitive to a spectral phase randomization of the signals. The latter implies that the natural visibility graph is able to capture nonlinearities in the signal, as linear effects are preserved during phase randomization (i.e. amplitude spectrum does not change) while nonlinearities are lost through phase shuffling. We stress that the visibility networks do not require any *a priori* parameters and are directly built from the full velocity signals (instead of the small-scale component), because the network degree is

able to capture the signal structure at the local scales. In this regard, although in this work a one-point analysis is carried out for simplicity, a two-point analysis (where the large-scale signal is extracted at a fixed wall-normal coordinate) would reveal the full potential of visibility networks. In fact, when multiple synchronized signals are available at different wall-normal locations (e.g. from numerical simulations, hot-wire rakes or through particle image velocimetry), the large-scale signal can be obtained only once at a fixed wall-normal location, and probes working on a smaller frequency range can be employed (as only low-frequencies are necessary). The full velocity signals, instead, can be used without any filtering operation to capture the small-scales frequency modulation at the remaining wall-normal locations.

In the wake of the recent successful applications of network science to the analysis of turbulent flows (Murugesan & Sujith 2015; Taira, Nair & Brunton 2016; Schlueter-Kuck & Dabiri 2017; Iacobello *et al.* 2019*b*; Krishnan *et al.* 2019), the proposed visibility-based approach is a candidate as a parameter-free and robust tool for FM investigation.

Declaration of interests. The authors report no conflict of interest.

Author ORCIDs.
Giovanni Iacobello https://orcid.org/0000-0002-0954-8545.

Appendix A. Synthetic signals for visibility-based FM detection

In this appendix, we provide the results of the application of the visibility-based approach to quantify FM from synthetic signals, which is a simple but representative benchmark of more complex signals such as those from turbulent flow fields. Three configurations of modulation are here investigated, as shown in figure 9(*a–c*), namely amplitude modulation (AM), frequency modulation (FM) and both amplitude and frequency modulation (AM+FM). In this way, we assess the effect of different modulations on the ratio K_{np} and its ability to discern FM only.

All the generated signals have length $N = 10^4$ and sampling frequency $f_{samp} = 4000$ Hz, which is chosen to be much larger than the characteristic frequencies of the modulated and modulating signals. The modulating (i.e. large-scale) signal, shown in red in figure 9(*a–c*), is given by the expression $s_L(t_i) = \cos(2\pi f_L t_i)/3$, where $t_i = (i-1)/f_{samp}$ is the time, with $i = 1, \ldots, N$, and $f_L = 2$ Hz is the frequency of the modulating signal.

The three modulated signals, s_{AM}, s_{FM} and s_{AFM}, are constructed as a high-frequency sinusoidal series, which emulate the small-scale velocity component, modulated by s_L. A positive modulation is considered, namely, an increase of amplitude and/or frequency is induced for intervals of positive s_L values and *vice versa* for negative s_L values. This behaviour mimics the modulation close to the wall by the large scales to the small scales in wall-bounded turbulence. Specifically, the three modulated signals, shown as black lines in figure 9(*a–c*), are given as

(i) $s_{AM} = (\cos[2\pi f_H t_i] + s_R)(1 + s_L)$;
(ii) $s_{FM} = \cos[2\pi f_H t_i + \varphi_L] + s_R$; and
(iii) $s_{AFM} = s_{FM}(1 + s_L)$,

where $f_H = 12$ Hz is the (high) carrier-frequency of the modulated signals. The role of $(1 + s_L)$ is to provide the AM effect on s_{AM} and s_{AFM}, while the role of φ_L is to give a frequency-modulated component to s_{FM} and s_{AFM}. In particular, φ_L is a time-varying phase depending on s_L typically used to generate frequency-modulated signals (Boashash 2015), defined as $\varphi_L = 2\pi f_\Delta I_m$, where $f_\Delta = 11$ Hz is the frequency deviation (i.e. the maximum

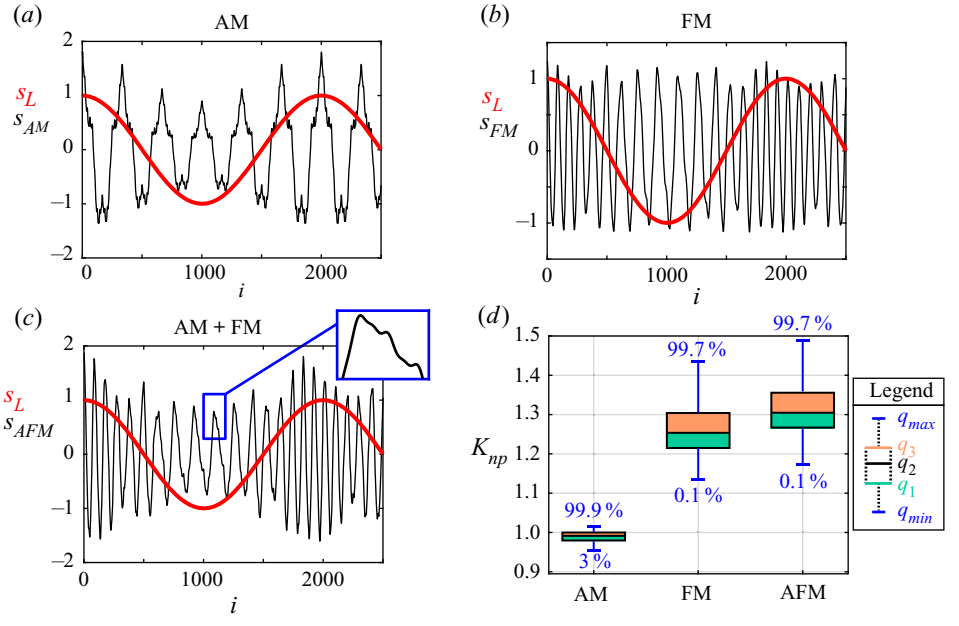

Figure 9. First 2500 time instants (out of 10^4) of the three synthetic modulated signals (shown in black) and the modulating signal (shown in red) for: (*a*) amplitude modulated signal (shown as AM); (*b*) frequency modulated signal (shown as FM); (*c*) amplitude and frequency modulated signal (shown as AM+FM). The inset shows a zoom of the AM+FM modulated signal. (*d*) Results of the application of the NVG to the synthetic signals in (*a–c*). Values of K_{np} are shown as box plots, where q_1, q_2 and q_3 are the 25th, median, and 75th percentiles, respectively, while $q_{min} = q_1 - 1.5(q_3 - q_1)$ and $q_{max} = q_1 + 1.5(q_3 - q_1)$, whose values are explicitly indicated at the tips of the whiskers as percentages.

frequency shift from f_H) and $I_m \equiv \sum_i s_L(t_i)/f_{samp}$. The frequency deviation, f_Δ, is selected to be close to the value of the carrier frequency, f_H, to maximize the modulation effect on the signal.

In each of the three modulated series, an additional signal, s_R, is also included. It is obtained as a sum of unmodulated cosine signals with randomly-varying amplitude, given by

$$s_R(t_i) = \sum_{q=2}^{5} \frac{r_A}{2^q} \cos[2\pi(2^q f_H)t_i], \tag{A1}$$

where r_A is a random number extracted from a uniform distribution in the range (0, 1). The effect of s_R in a modulated signal can be observed in the inset of figure 9(*c*). The role of s_R is to introduce – similar to turbulence velocity spectra – additional high-frequency low-amplitude components, thus making the modulated (small-scale) signal a broadband-like series.

By generating several random amplitudes, r_A, in (A1), an ensemble of s_R series is obtained for each r_A. This leads to an ensemble of different modulated signals, s_{AM}, s_{FM} and s_{AFM}, which are characterized by different s_R. Specifically, we generated 5×10^3 values of r_A for each of the three modulated signals. The values of the ratio K_{np} (see (2.3*a–c*)) are then computed for each ensemble, by evaluating the degree on the NVGs built for the full signals, namely, $(s_{AM} + s_L)$, $(s_{FM} + s_L)$ and $(s_{AFM} + s_L)$.

Figure 9(*d*) shows the values of K_{np} for the three modulation configurations as box plots, in which the most significant percentiles are highlighted. For the AM case, K_{np} is

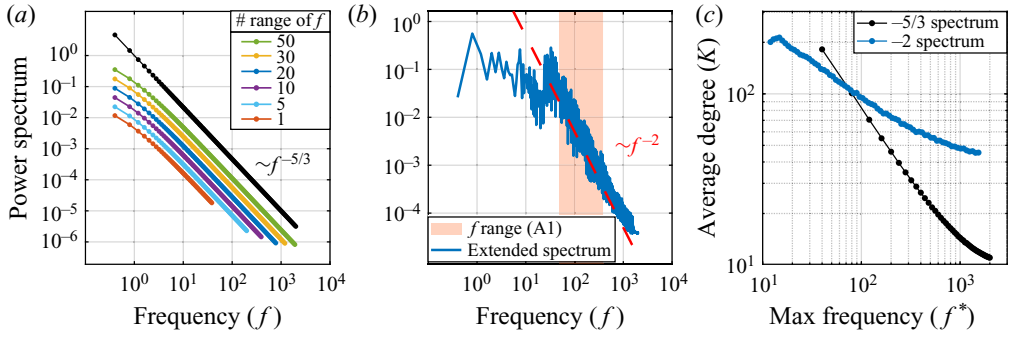

Figure 10. (*a*) Power spectra of synthetic signals following a $f^{-5/3}$ law. Signals are generated through inverse-Fourier transform of the power spectrum shown in black for different frequency ranges (i.e. different number of harmonics). Fifty ranges of f are generated, and the spectra of the synthetic signals for some representative f ranges are highlighted with different colours, as well as vertically shifted to enhance visualization. (*b*) Power spectrum of signals generated as per (A1). The range of frequencies considered for the (A1) is highlighted as a shaded red region, and an f^{-2} scaling is also shown. (*c*) Average degree centrality, K, for signals generated as in (*a*,*b*) for increasing maximum frequency, f^*.

concentrated around unity, with a median value that is very close to one, as is expected because the main modulating effect is on the amplitude. For the FM and AFM cases, instead, values of K_{np} greater than one are consistently obtained (note the percentile values in figure 9*d*), as a result of the positive frequency modulating effect of the large-scale signal. In particular, it is worth noting that even when a signal is modulated both in amplitude and frequency, the ratio K_{np} is able to emphasize the contribution of the FM.

The results shown in figure 9(*d*) reveal that K_{np} is an accurate parameter to quantify FM, because it consistently shows positive values under positive FM, and also a precise metric, because there is narrow spreading of the K_{np} values around the median. The results shown in this appendix corroborate the ability and robustness of the proposed visibility-based approach, which relies on the conditioned degree centrality, to capture frequency modulation, thus fostering its application as a tool to study scale interaction in wall-bounded turbulence.

To conclude this section, we show the effect of higher frequency harmonics on the average degree, K, for synthetic signals. With this aim, we use two sets of synthetic signals according to their power spectrum scaling following: (i) a $-5/3$ spectrum; and (ii) a -2 spectrum. The former emulates turbulent signals in the inertial range, while the second refers to signals defined in (A1). Figure 10(*a*,*b*) shows the power spectra for both types of synthetic signals, while figure 10(*c*) illustrates the behaviour of K as a function of the maximum frequency considered, f^*. As discussed in § 2.2 referring to figure 3(*c*) for a turbulent series, K decreases as the number of high-frequency harmonics increases. Moreover, the changes in K are stronger for the synthetic signals following the $f^{-5/3}$ spectrum (figure 10*a*) than for the f^{-2} spectrum (figure 10*b*), because the energy content of the small scales is larger in the former case, as the exponent $-5/3$ is lower (in modulus) than -2.

Appendix B. Sensitivity analysis

The aim of this section is to assess the robustness of the proposed NVG-based approach under different values of the spectral filtering wavelength and under high-frequency noise.

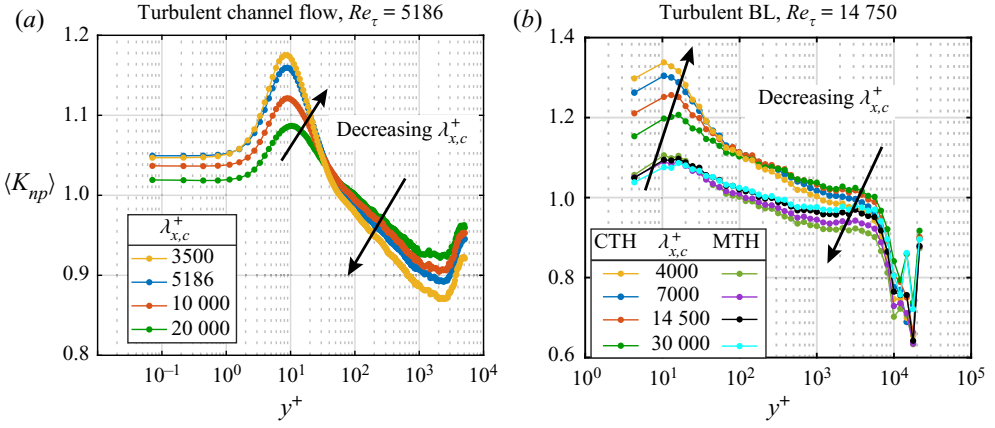

Figure 11. Effect of different cut-off wavelengths in the large-scale conditional average degree ratio, $K_{np}(y^+)$, for streamwise velocity, u, extracted from (*a*) the channel flow DNS at $Re_\tau \approx 5200$ and (*b*) the boundary layer experiments. In (*b*), the cut-off effect for spatial series obtained from the time series via the CTH, namely using as convection velocity the local mean velocity, and the MTH. Angular brackets indicate averaging over time and spanwise direction in (*a*) and over three different realizations in (*b*).

We recall that the spectral filtering wavelength is used to extract the large-scale component, u_{LS}, from the streamwise velocity signal, u. Mathis *et al.* (2009*a*) first reported a sensitivity analysis on the AM of streamwise velocity in a turbulent boundary layer. They showed that a decrease of the cut-off wavelength leads to a small increase of the AM below the reversal wall-normal coordinate (i.e. in the near-wall region) and a small decrease of AM above the reversal coordinate (i.e. far from the wall). The conclusion was that, despite the small variations arising from different cut-off wavelengths, the general form of the AM parameter is retained. For this reason, subsequent works on AM and FM exploited the sensitivity analysis by Mathis *et al.* (2009*a*) as a reference case to justify the choice of the cut-off wavelength.

Here we perform a sensitivity analysis on the wall-normal behaviour of K_{np} for the streamwise velocity by changing the cut-off wavelength, $\lambda_{x,c}$. Figure 11 shows K_{np} as a function of y^+ for four $\lambda_{x,c}$ values, in the turbulent channel flow at $Re_\tau \approx 5200$ (figure 11(*a*), $\lambda^+_{x,c} = 5186$ in the main text) and the turbulent boundary layer (figure 11(*b*), $\lambda^+_{x,c} = 7000$ in the main text). For the boundary layer, both the classical and modified Taylor's hypotheses are considered and labelled as CTH and MTH in the legend of figure 11(*b*). The nominal shape of K_{np} as a function of y^+ is maintained for both the channel and boundary layers setups, and – similar to the analysis carried out by Mathis *et al.* (2009*a*) – a decrease in $\lambda_{x,c}$ leads to a reduction of K_{np} below the reversal y^+ and a rise of K_{np} above the reversal y^+. Specifically, variations of K_{np} in the wall proximity are less evident for the boundary layer when the MTH is applied rather than when local mean velocity is considered as convection velocity (CTH).

This sensitivity analysis confirms the robustness of the decoupling procedure to extract u_{LS}, which is employed to evaluate K_{np} as a metric for studying the FM.

Finally, our method is tested with the presence of high-frequency noise in the velocity signals (as usually happens in experimental measurements). With this aim, high-frequency noise is artificially added to the experimental signals of the streamwise velocity (whose sampling frequency is $f_s = 20\,000$ Hz) in the turbulent boundary layer. The noise signal is given by the sum of three harmonics with random phase and with frequencies equal to

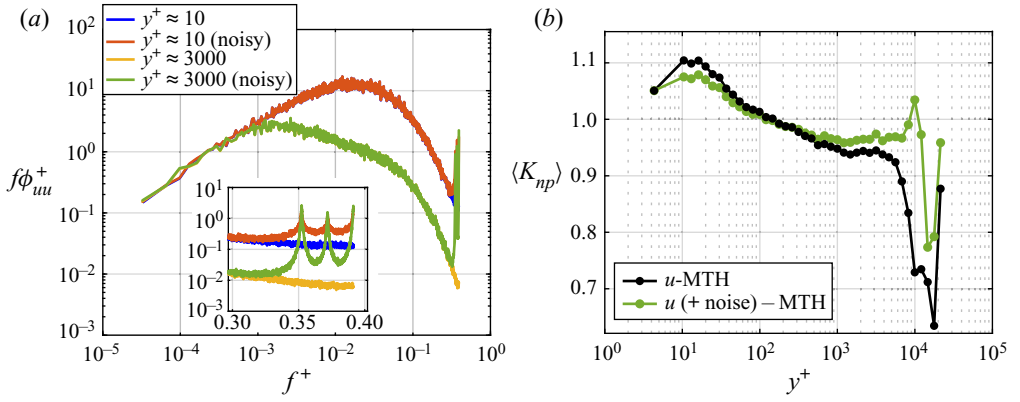

Figure 12. (*a*) Pre-multiplied energy spectrum of the streamwise velocity, *uu*, from the turbulent boundary layer at two representative y^+ locations with and without high-frequency noise. The inset shows a zoom at the highest frequencies. (*b*) The K_{np} as a function of y^+ for velocity signals without (black) and with (green) high-frequency noise (the MTH is used).

$0.5f_s$, $0.475f_s$ and $0.45f_s$ (the maximum frequency included is $f_s/2$ as higher frequencies are not captured in the amplitude spectrum), whose effects on the spectra are displayed in figure 12(*a*). The corresponding values of K_{np} are shown in figure 12(*b*), where we observe that the behaviour of K_{np} is retained throughout the boundary layer except for the intermittency region, where the noise intensity significantly affects the signal structure. Therefore, we conclude that, although a pre-processing of the (experimental) data is always a good practice to avoid biased behaviours, the NVG approach based on K_{np} is sufficiently robust under high-frequency noise.

References

Agostini, L. & Leschziner, M. 2014 On the influence of outer large-scale structures on near-wall turbulence in channel flow. *Phys. Fluids* **26** (7), 075107.

Agostini, L. & Leschziner, M. 2016 Predicting the response of small-scale near-wall turbulence to large-scale outer motions. *Phys. Fluids* **28** (1), 015107.

Agostini, L. & Leschziner, M. 2019 On the departure of near-wall turbulence from the quasi-steady state. *J. Fluid Mech.* **871**, R1.

Agostini, L., Leschziner, M. & Gaitonde, D. 2016 Skewness-induced asymmetric modulation of small-scale turbulence by large-scale structures. *Phys. Fluids* **28** (1), 015110.

Anderson, W. 2016 Amplitude modulation of streamwise velocity fluctuations in the roughness sublayer: evidence from large-eddy simulations. *J. Fluid Mech.* **789**, 567–588.

Awasthi, A. & Anderson, W. 2018 Numerical study of turbulent channel flow perturbed by spanwise topographic heterogeneity: amplitude and frequency modulation within low-and high-momentum pathways. *Phys. Rev. Fluids* **3** (4), 044602.

Baars, W.J., Hutchins, N. & Marusic, I. 2016 Spectral stochastic estimation of high-Reynolds-number wall-bounded turbulence for a refined inner-outer interaction model. *Phys. Rev. Fluids* **1** (5), 054406.

Baars, W.J., Hutchins, N. & Marusic, I. 2017 Reynolds number trend of hierarchies and scale interactions in turbulent boundary layers. *Phil. Trans. R. Soc.* A **375** (2089), 20160077.

Baars, W.J., Talluru, K.M., Hutchins, N. & Marusic, I. 2015 Wavelet analysis of wall turbulence to study large-scale modulation of small scales. *Exp. Fluids* **56** (10), 188.

Balakumar, B.J. & Adrian, R.J. 2007 Large-and very-large-scale motions in channel and boundary-layer flows. *Phil. Trans. R. Soc.* A **365** (1852), 665–681.

Bandyopadhyay, P.R. & Hussain, A.K.M.F. 1984 The coupling between scales in shear flows. *Phys. Fluids* **27** (9), 2221–2228.

Basley, J., Perret, L. & Mathis, R. 2018 Spatial modulations of kinetic energy in the roughness sublayer. *J. Fluid Mech.* **850**, 584–610.

Bernardini, M. & Pirozzoli, S. 2011 Inner/outer layer interactions in turbulent boundary layers: a refined measure for the large-scale amplitude modulation mechanism. *Phys. Fluids* **23** (6), 061701.

Boashash, B. 2015 *Time-Frequency Signal Analysis and Processing: A Comprehensive Reference*. Academic Press.

Brown, G.L. & Thomas, A.S.W. 1977 Large structure in a turbulent boundary layer. *Phys. Fluids* **20** (10), S243–S252.

Charakopoulos, A.K., Karakasidis, T.E., Papanicolaou, P.N. & Liakopoulos, A. 2014 The application of complex network time series analysis in turbulent heated jets. *Chaos* **24** (2), 024408.

Chernyshenko, S. 2020 Extension of QSQH theory of scale interaction in near-wall turbulence to all velocity components. arXiv:2002.05585.

Chung, D. & McKeon, B.J. 2010 Large-eddy simulation of large-scale structures in long channel flow. *J. Fluid Mech.* **661**, 341–364.

Dogan, E., Örlü, R., Gatti, D., Vinuesa, R. & Schlatter, P. 2019 Quantification of amplitude modulation in wall-bounded turbulence. *Fluid Dyn. Res.* **51** (1), 011408.

Duvvuri, S. & McKeon, B.J. 2015 Triadic scale interactions in a turbulent boundary layer. *J. Fluid Mech.* **767**, R4.

Fiscaletti, D., Attili, A., Bisetti, F. & Elsinga, G.E. 2016 Scale interactions in a mixing layer – the role of the large-scale gradients. *J. Fluid Mech.* **791**, 154–173.

Fiscaletti, D., Ganapathisubramani, B. & Elsinga, G.E. 2015 Amplitude and frequency modulation of the small scales in a jet. *J. Fluid Mech.* **772**, 756–783.

Ganapathisubramani, B., Hutchins, N., Monty, J.P., Chung, D. & Marusic, I. 2012 Amplitude and frequency modulation in wall turbulence. *J. Fluid Mech.* **712**, 61–91.

Graham, J., *et al.* 2016 A web services accessible database of turbulent channel flow and its use for testing a new integral wall model for LES. *J. Turbul.* **17** (2), 181–215.

Guala, M., Metzger, M. & McKeon, B.J. 2011 Interactions within the turbulent boundary layer at high Reynolds number. *J. Fluid Mech.* **666**, 573–604.

Hasson, U., Iacovacci, J., Davis, B., Flanagan, R., Tagliazucchi, E., Laufs, H. & Lacasa, L. 2018 A combinatorial framework to quantify peak/pit asymmetries in complex dynamics. *Sci. Rep.* **8** (1), 1–17.

Hu, R. & Zheng, X. 2018 Energy contributions by inner and outer motions in turbulent channel flows. *Phys. Rev. Fluids* **3** (8), 084607.

Huang, N.E., Shen, Z., Long, S.R., Wu, M.C., Shih, H.H., Zheng, Q., Yen, N.C., Tung, C.C. & Liu, H.H. 1998 The empirical mode decomposition and the Hilbert spectrum for nonlinear and non-stationary time series analysis. *Proc. R. Soc. Lond.* A **454** (1971), 903–995.

Hutchins, N. 2014 Large-scale structures in high Reynolds number wall-bounded turbulence. In *Progress in Turbulence V - iTi 2018* (ed. A. Talamelli, M. Oberlack & J. Peinke), pp. 75–83. Springer.

Hutchins, N. & Marusic, I. 2007*a* Evidence of very long meandering features in the logarithmic region of turbulent boundary layers. *J. Fluid Mech.* **579**, 1–28.

Hutchins, N. & Marusic, I. 2007*b* Large-scale influences in near-wall turbulence. *Phil. Trans. R. Soc.* A **365** (1852), 647–664.

Hwang, J., Lee, J., Sung, H.J. & Zaki, T.A. 2016 Inner–outer interactions of large-scale structures in turbulent channel flow. *J. Fluid Mech.* **790**, 128–157.

Iacobello, G. 2020 Fast natural visibility graph (NVG) for MATLAB. *MATLAB Central File Exchange*.

Iacobello, G., Marro, M., Ridolfi, L., Salizzoni, P. & Scarsoglio, S. 2019*a* Experimental investigation of vertical turbulent transport of a passive scalar in a boundary layer: statistics and visibility graph analysis. *Phys. Rev. Fluids* **4** (10), 104501.

Iacobello, G., Ridolfi, L., Marro, M., Salizzoni, P. & Scarsoglio, S. 2018*a* Complex network analysis of wind tunnel experiments on the passive scalar dispersion in a turbulent boundary layer. In *Progress in Turbulence VIII - iTi 2018* (ed. R. Örlü, A. Talamelli, J. Peinke & M. Oberlack), pp. 215–220. Springer.

Iacobello, G., Ridolfi, L. & Scarsoglio, S. 2021 A review on turbulent and vortical flow analyses via complex networks. *Physica* A **563**, 125476.

Iacobello, G., Scarsoglio, S., Kuerten, J.G.M. & Ridolfi, L. 2019*b* Lagrangian network analysis of turbulent mixing. *J. Fluid Mech.* **865**, 546–562.

Iacobello, G., Scarsoglio, S. & Ridolfi, L. 2018*b* Visibility graph analysis of wall turbulence time-series. *Phys. Lett.* A **382** (1), 1–11.

Jiménez, J. 2018 Coherent structures in wall-bounded turbulence. *J. Fluid Mech.* **842**, P1.

KRISHNAN, A., SUJITH, R.I., MARWAN, N. & KURTHS, J. 2019 On the emergence of large clusters of acoustic power sources at the onset of thermoacoustic instability in a turbulent combustor. *J. Fluid Mech.* **874**, 455–482.

LACASA, L. & IACOVACCI, J. 2017 Visibility graphs of random scalar fields and spatial data. *Phys. Rev.* E **96** (1), 012318.

LACASA, L., LUQUE, B., BALLESTEROS, F., LUQUE, J. & NUNO, J.C. 2008 From time series to complex networks: the visibility graph. *Proc. Natl Acad. Sci.* **105** (13), 4972–4975.

LEE, M. & MOSER, R.D. 2015 Direct numerical simulation of turbulent channel flow up to $Re_\tau \approx 5200$. *J. Fluid Mech.* **774**, 395–415.

LI, Y., PERLMAN, E., WAN, M., YANG, Y., MENEVEAU, C., BURNS, R., CHEN, S., SZALAY, A. & EYINK, G. 2008 A public turbulence database cluster and applications to study Lagrangian evolution of velocity increments in turbulence. *J. Turbul.* **9**, N31.

LIU, C., ZHOU, W.X. & YUAN, W.K. 2010 Statistical properties of visibility graph of energy dissipation rates in three-dimensional fully developed turbulence. *Physica* A **389** (13), 2675–2681.

LUQUE, B., LACASA, L., BALLESTEROS, F. & LUQUE, J. 2009 Horizontal visibility graphs: exact results for random time series. *Phys. Rev.* E **80** (4), 046103.

MARUSIC, I. 2020 Two-point high Reynolds number zero-pressure gradient turbulent boundary layer dataset. doi:10.26188/5e919e62e0dac.

MARUSIC, I. & HEUER, W.D.C. 2007 Reynolds number invariance of the structure inclination angle in wall turbulence. *Phys. Rev. Lett.* **99** (11), 114504.

MARUSIC, I., MATHIS, R. & HUTCHINS, N. 2010 Predictive model for wall-bounded turbulent flow. *Science* **329** (5988), 193–196.

MATHIS, R., HUTCHINS, N. & MARUSIC, I. 2009*a* Large-scale amplitude modulation of the small-scale structures in turbulent boundary layers. *J. Fluid Mech.* **628**, 311–337.

MATHIS, R., HUTCHINS, N. & MARUSIC, I. 2011 A predictive inner–outer model for streamwise turbulence statistics in wall-bounded flows. *J. Fluid Mech.* **681**, 537–566.

MATHIS, R., MARUSIC, I., CHERNYSHENKO, S.I. & HUTCHINS, N. 2013 Estimating wall-shear-stress fluctuations given an outer region input. *J. Fluid Mech.* **715**, 163–180.

MATHIS, R., MONTY, J.P., HUTCHINS, N. & MARUSIC, I. 2009*b* Comparison of large-scale amplitude modulation in turbulent boundary layers, pipes, and channel flows. *Phys. Fluids* **21** (11), 111703.

MONTY, J.P., HUTCHINS, N., NG, H.C.H., MARUSIC, I. & CHONG, M.S. 2009 A comparison of turbulent pipe, channel and boundary layer flows. *J. Fluid Mech.* **632**, 431–442.

MONTY, J.P., STEWART, J.A., WILLIAMS, R.C. & CHONG, M.S. 2007 Large-scale features in turbulent pipe and channel flows. *J. Fluid Mech.* **589**, 147–156.

MURUGESAN, M. & SUJITH, R.I. 2015 Combustion noise is scale-free: transition from scale-free to order at the onset of thermoacoustic instability. *J. Fluid Mech.* **772**, 225–245.

MURUGESAN, M. & SUJITH, R.I. 2016 Detecting the onset of an impending thermoacoustic instability using complex networks. *J. Propul. Power* **32** (3), 707–712.

MURUGESAN, M., ZHU, Y. & LI, L.K.B. 2019 Complex network analysis of forced synchronization in a hydrodynamically self-excited jet. *Intl J. Heat Fluid Flow* **76**, 14–25.

NEWMAN, M. 2018 *Networks*, 2nd edn. Oxford University Press.

PATHIKONDA, G. & CHRISTENSEN, K.T. 2017 Inner–outer interactions in a turbulent boundary layer overlying complex roughness. *Phys. Rev. Fluids* **2** (4), 044603.

PATHIKONDA, G. & CHRISTENSEN, K.T. 2019 Investigation of inner-outer interactions in a turbulent boundary layer using high-speed particle image velocimetry. *Phys. Rev. Fluids* **4** (3), 034607.

PERUZZI, C., POGGI, D., RIDOLFI, L. & MANES, C. 2020 On the scaling of large-scale structures in smooth-bed turbulent open-channel flows. *J. Fluid Mech.* **889**, A1.

SCHLATTER, P. & ÖRLÜ, R. 2010 Quantifying the interaction between large and small scales in wall-bounded turbulent flows: a note of caution. *Phys. fluids* **22** (5), 051704.

SCHLUETER-KUCK, K.L. & DABIRI, J.O. 2017 Coherent structure colouring: identification of coherent structures from sparse data using graph theory. *J. Fluid Mech.* **811**, 468–486.

SINGH, J., BELUR VISHWANATH, R., CHAUDHURI, S. & SUJITH, R.I. 2017 Network structure of turbulent premixed flames. *Chaos* **27** (4), 043107.

SMITS, A.J., MCKEON, B.J. & MARUSIC, I. 2011 High–Reynolds number wall turbulence. *Annu. Rev. Fluid Mech.* **43**, 353–375.

SQUIRE, D.T., BAARS, W.J., HUTCHINS, N. & MARUSIC, I. 2016 Inner–outer interactions in rough-wall turbulence. *J. Turbul.* **17** (12), 1159–1178.

TAIRA, K., NAIR, A.G. & BRUNTON, S.L. 2016 Network structure of two-dimensional decaying isotropic turbulence. *J. Fluid Mech.* **795**, R2.

TALLURU, K.M., BAIDYA, R., HUTCHINS, N. & MARUSIC, I. 2014 Amplitude modulation of all three velocity components in turbulent boundary layers. *J. Fluid Mech.* **746**, R1.

TANG, Z. & JIANG, N. 2018 Scale interaction and arrangement in a turbulent boundary layer perturbed by a wall-mounted cylindrical element. *Phys. Fluids* **30** (5), 055103.

TOKAMI, T., HACHIJO, T., MIYANO, T. & GOTODA, H. 2020 Spatiotemporal dynamics of a buoyancy-driven turbulent fire. *Phys. Rev.* E **101** (4), 042214.

WU, S., CHRISTENSEN, K.T. & PANTANO, C. 2019 Modelling smooth-and transitionally rough-wall turbulent channel flow by leveraging inner–outer interactions and principal component analysis. *J. Fluid Mech.* **863**, 407–453.

YANG, X.I.A. & HOWLAND, M.F. 2018 Implication of Taylor's hypothesis on measuring flow modulation. *J. Fluid Mech.* **836**, 222–237.

YAO, Y.C., HUANG, W.X. & XU, C.X. 2018 Amplitude modulation and extreme events in turbulent channel flow. *Acta Mechanica Sin.* **34** (1), 1–9.

ZHANG, C. & CHERNYSHENKO, S.I. 2016 Quasisteady quasihomogeneous description of the scale interactions in near-wall turbulence. *Phys. Rev. Fluids* **1** (1), 014401.

ZHUANG, E., SMALL, M. & FENG, G. 2014 Time series analysis of the developed financial markets' integration using visibility graphs. *Physica* A **410**, 483–495.

ZOU, Y., DONNER, R.V., MARWAN, N., DONGES, J.F. & KURTHS, J. 2018 Complex network approaches to nonlinear time series analysis. *Phys. Rep.* **787**, 1–97.